Modelling Blue Straggler Populations with BPASS

A thesis submitted in fulfilment of the requirements for the degree of

Masters of Science in Physics, The University of Auckland, 2022

Gleb Geinke

Acknowledgements

I would like to thank my supervisor and co-supervisor, Associate Professor J. J. Eldridge and Dr. Heloise Stevance, for their help directing and educating me while writing this thesis and throughout every stage of my studies. This thesis would not be possible without their guidance and the opportunity to work closely with them on their projects BPASS and `hoki`. A special thanks to everyone else on Stars'n'Supernovae team: Sean Richards, Max Briel, Sohan Ghodla, Petra Tang, Wouter van Zeist and others, who helped throughout the year and provided valuable suggestions and opinions.

Thanks to Mr. Roger, my high-school physics teacher, for sparking my interest for physics, and to all the professors at the University of Auckland for continuing it.

And finally I would like to thank my family and especially my partner, Grace Wright, for the moral support through the year!

Abstract

Most binary population synthesis models fail to predict Blue Straggler populations accurately, largely underpredicting the ratio of Blue Stragglers to Red Giants. Binary interaction and mass-transfer are key processes in the formation of Blue Stragglers and therefore they are a sensitive test for the mass-transfer stability of binary models. This thesis tests predictions by BPASS (Binary Population and Spectral Synthesis) models for Blue Straggler populations. Results show that binary systems with primary stars in the $1 M_\odot$ to $2 M_\odot$ mass range are the major contributors to the increase of Blue Stragglers from log(age/yrs)=9 to log(age/yrs)=10. A comparison of observational data to BPASS models shows agreement with Blue Stragglers/Red Giants ratio within the margin of error, much closer than other population synthesis models. We find that this is due to the stellar structure evolving in detail throughout the mass-transfer. This results in more stable mass-transfer events than is estimated with rapid evolution codes. Understanding mass transfer in these low mass stars is important for a variety of aspects of astrophysics, for example, in the formation of type Ia supernovae through the single-degenerate scenario. We suggest the next step in this project would be to explore this pathway as well as study a greater sample of old stellar populations to constrain the models of mass transfer to a greater degree.

Contents

---

[1]https://bpass.auckland.ac.nz/

[2]https://heloises.github.io/hoki/CMDs.html

List of Figures

List of Tables

Glossary of Terms

ABBREVIATION	DESCRIPTION
BPASS	Binary Population and Spectral Synthesis code.
HRD	Hertzsprung-Russel Diagram.
CMD	Colour Magnitude Diagram.
BSS	Blue Straggler Star.
RGB	Red Giant Branch.
MSTO	Main Sequence Turnoff.
COSMIC	Compact Object Synthesis and Monte Carlo Investigation Code.

Notation

SYMBOL   **MEANING**

$M_{\odot}$ Solar Mass.

M_c Mass of the Star's Core.

Z Metallicity.

N_{BSS} Number of Blue Straggler Stars.

N_{RGB} Number of Red Giant Stars.

R_L Roche-Lobe Radius.

---

1 Introduction

Astronomical observations date back as far as 1800 BCE. The Nebra Sky Disc, estimated to be from the Bronze Age, depicts the Sun, moon and stars, including the star cluster Pleiades, which is still studied to this day (Pásztor, 2015). The desire to explore space to answer some of humanity's largest questions, like "How did everything begin?" or "Are we unique in the Universe?" has always been part of human nature. In ∼1700 BCE, Babylonians recorded planet motions and star constellations for astronomical predictions (Verderame, 2001). In 400-100 BCE Greeks proposed models of our solar system and created the first astro-numerical computer with the Antikythera mechanism, which was incredibly precise for its time and was the pinnacle of engineering, mathematical and astronomical knowledge (Efstathiou & Efstathiou, 2018). In 1687, Sir Isaac Newton developed the universal law of gravity, allowing us to predict the motion of planets accurately, and shaping the science of astrophysics as we know it now.

In the 17th century William Herschel, who surveyed and discovered over 1000 nebulae (bright gaseous clouds of dust) over 20 years, was one of the first to propose that stars form in these clouds of gas (Britannica, Britannica). He hypothesised that stars formed in the nebulae eventually pull closer together and form star clusters, suggesting that stars in clusters are of similar composition and age. This played a great role in our understanding of stellar evolution when later, in 1910, Hans Rosenberg and Ejnar Hertzsprung published a scatter plot of the temperature and spectral type or luminosity of the Pleiades star cluster (Rosenberg, 1910). This plot, later named the Hertzsprung-Russel diagram (HRD), showed the main stages of evolution of stars, which are discussed in Section 1.1. A typical HRD is given in Fig. 1.1. This was the key to realise that most stars are so-called main sequence stars, with the next most populous grouping being the red giants, while other stars are more unique. We describe the main sequence, red giant and other phases in Section 1.1. For a few decades after 1910, it was believed that mass is the main factor in the evolution of stars, and when looking at a cluster, more massive stars would be giants and subgiants, while low mass stars of the same age are still on the main sequence. There was an exception to this named an Algol paradox where a binary system had the smaller star being a red giant and the bigger star was still on the main sequence. As more observations were collected, more stars were found whose evolution could not be explained.
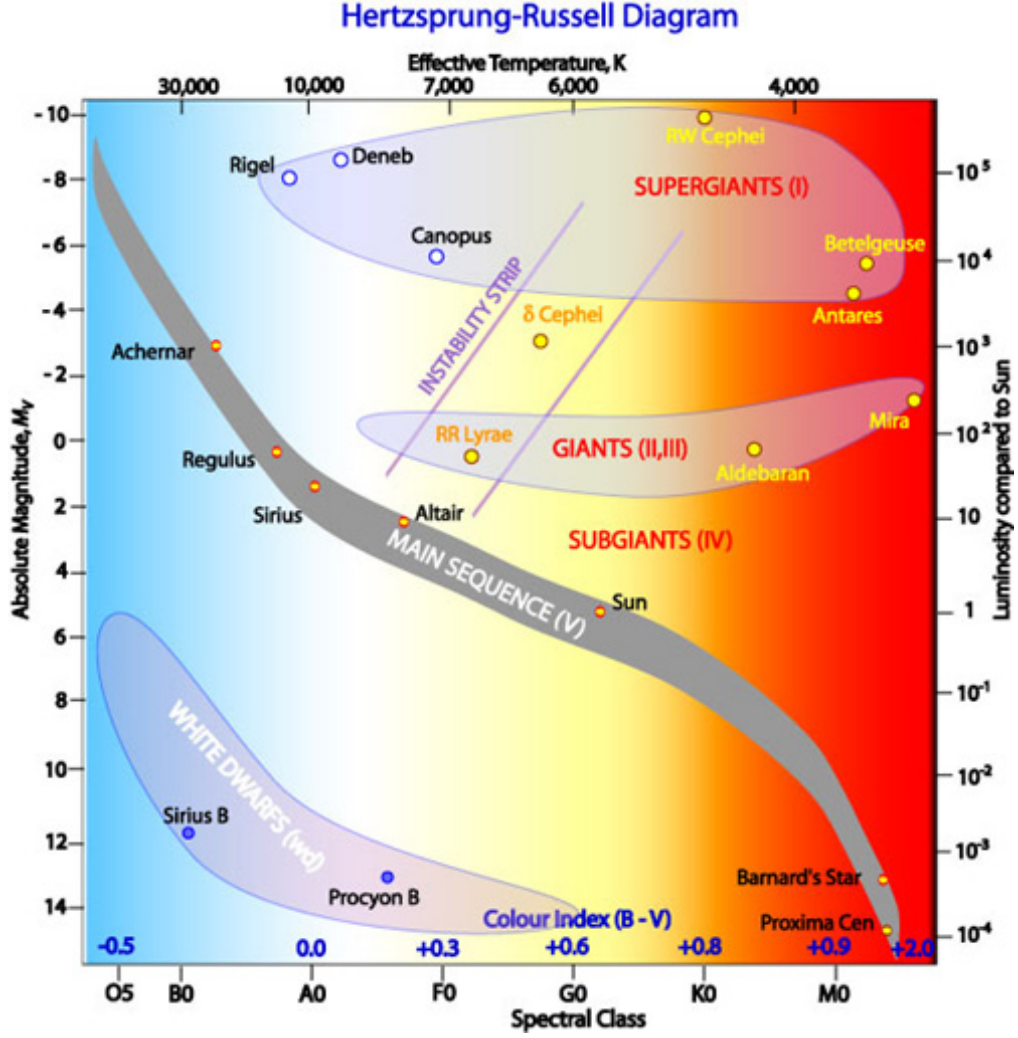
Figure 1.1: Hertzsprung-Russel Diagram showing various stages of stellar evolution. (Hollow, 2022)

Binary stars differ from single stars in their evolution. For the most part of their lifetime, all stars evolve on their own, but if the primary star (most massive one) grows in radius enough to interact with a companion star, then part of the mass will be transferred. This alters the evolution of both stars, and the secondary can rejuvenate, becoming brighter, bluer and effectively younger than other stars in the same cluster. Hence the name for these stars, "blue stragglers".

This thesis focuses on blue stragglers and explores their mass transfer formation channels in detail using computational models. Better modelling of this mass transfer process in star clusters is important for our understanding of how other low mass binary products form, such as Type Ia supernovae and white dwarf systems (Leiner & Geller, 2021). A white dwarf is a remnant of a low-intermediate mass star, and Type Ia supernovae result from an explosion of a carbon-oxygen white dwarf when it exceeds $1.4 M_\odot$, and they are essential to nucleosynthesis. One channel for these events is where mass is transferred from a normal star onto a white dwarf, hence understanding such mass transfer is important to understand these supernovae. Which in turn is important to understand the source of elements produced in these explosions such as iron in the Universe.

1.1 Stellar evolution

With the evolution of technology, the number of observations of star clusters at all ages has increased significantly, which allows us to have a large sample of star clusters where blue stragglers are observed in populations with ages from 100 Myrs - 10 Gyrs. These ages correlate to intermediate-low mass stars in the range of $4.5M_\odot$ - $1M_\odot$, and to understand how the evolution of these stars is affected by mass transfer, one must know how they evolve on their own.

Stellar evolution is a complex process to model. Star lifetime starts from a hydrogen-rich molecular gas, which typically has a mass of multiple thousand solar masses. Parts of this cloud of gas collapse under self-gravity, forming denser clumps of gas, which consist of approximately 75% hydrogen, 25% helium and a few percent of heavier ionised elements like carbon and oxygen. Eventually, these clumps collapse under their own gravity, forming a protostar. It is a pre-stellar core that is still in the process of accreting dust and gas from around itself to grow in mass. As the mass grows, the protostar shrinks under the pressure becoming denser and hence increasing the internal temperature, and if the temperature reaches at least 10 million Kelvin, hydrogen burning begins. There are different reactions depending on the mass of the star that lead to different evolutionary paths. Below are three examples that examine what is going on inside of the star and the evolutionary path it takes - for a $1M_\odot$, $2.5M_\odot$ and $4.5M_\odot$ star. We also include a $10M_\odot$ star for comparison, but keep it brief as we are not concerned with details of high mass stars because they are outside of the mass range for blue stragglers and their donors within the scope of this study.

1.1.1 Low mass stars - $1M_\odot$ star

We begin our discussion of stellar evolution with a star of the same mass as our Sun. These stars have a lifetime of 9-10 Gyrs and represent the most long-lived stars we will consider in the study. Fig. 1.2 shows the evolution of the star, with the most interesting stages of evolution labeled and described in detail.
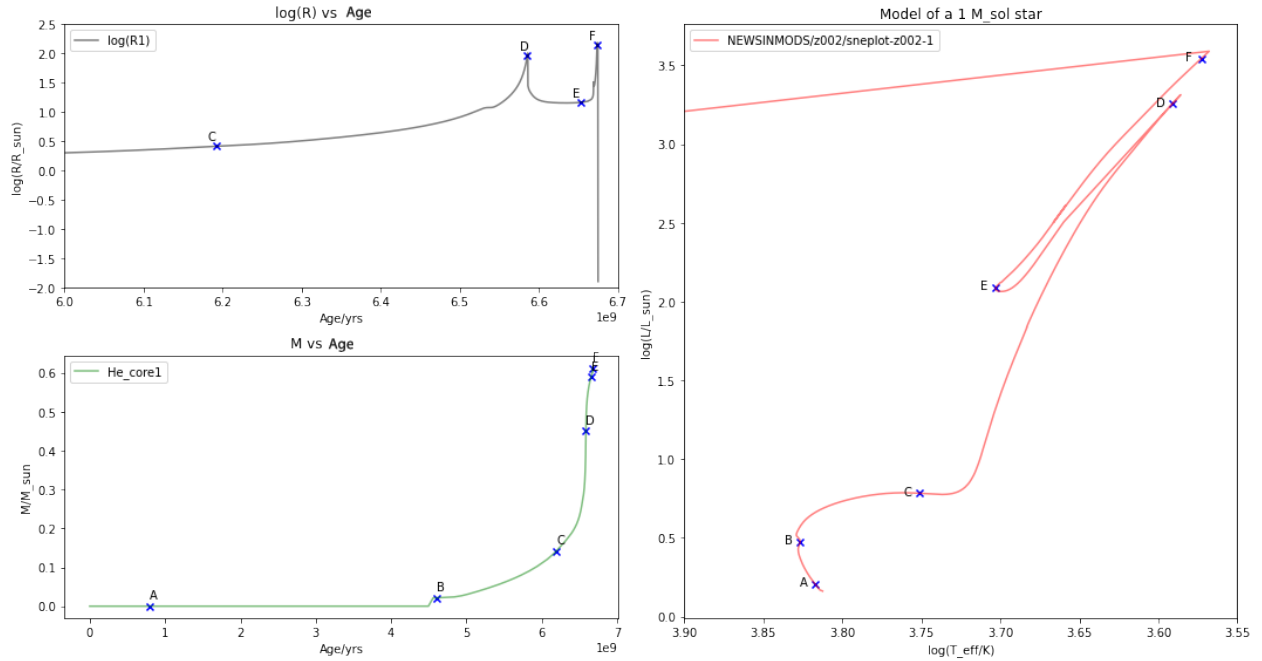
Figure 1.2: Plot on the right shows the evolution of a solar mass star on an H-R diagram that shows luminosity ($\log(L/L_\odot)$) against effective temperature ($\log(T_{\text{eff}}/K)$). Cross-points indicate important steps of evolution, where: A - pre-main sequence, B - top of the main sequence, C - Hertzsprung Gap, D/E/F - red giant branch. Top left plot shows the radius of the star with age, and bottom left plot shows the mass of the helium core with age.
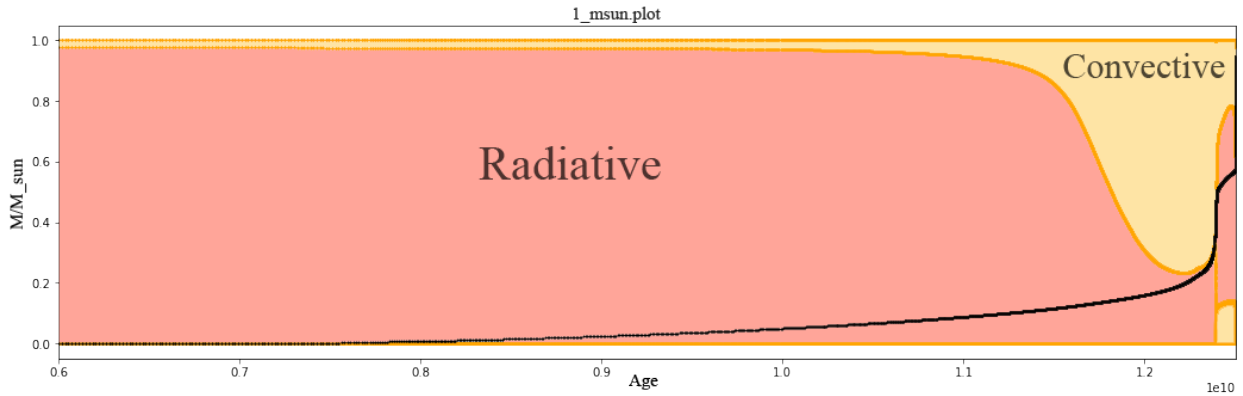
Figure 1.3: Internal structure of a $1M_\odot$ star showing the radiative and convective zones. Black line indicates the helium core. Age on the x-axis is slightly different to Fig. 1.2 due to different output files used.

A When the protostar accretes enough mass to start burning hydrogen it enters the zero-age main sequence stage (point A on Fig. 1.2). Stars spend 90% of their lifetime evolving on the main sequence, because hydrogen burning releases more energy than any other phase of nuclear fusion, therefore it can support the star's energy requirements for longer than any others. In a 1 $M_\odot$ star (and stars below 1.5 $M_\odot$ with $T_{\text{eff}} < 2 \times 10^7\ K$) the main source of energy is a process called a proton-proton chain (pp-chain). In this process, two hydrogen atoms are fused to produce deuterium - a one proton and one neutron isotope of hydrogen. As protons

4

fuse, one of them converts into a neutron, producing a positron and an electron neutrino. The positron reacts with an outer electron producing two gamma rays equivalent to approx. 1.4 MeV of thermal energy, so the full equation can be written as in the first equation in Table 1.1. Being the slowest reaction it determines the rate of hydrogen burning.

Further reaction in the chain is deuterium fusing with another hydrogen to gain one more proton in the nuclei and one more electron creating helium-3. The energy released while fusing to helium-3 is 5.49 MeV. So the total energy required to create helium-3 is 6.89 MeV. Helium-3 is then fused with another helium-3 to get one helium (^4He) and 2 hydrogen atoms releasing 12.86 MeV (Table 1.1 PP-I). Therefore the total energy output to receive one helium atom from hydrogen is $6.89 + 6.89 + 12.86 = 26.64$ MeV, and in our Sun this happens approximately 10^{38} times a second to produce the Sun's luminosity of 3.828×10^{26}W. This chain of reactions to produce helium accounts for approximately 85% of helium made in our Sun and is dominant for temperatures below 1.4×10^7K; it is generally called the pp-I branch. As more helium accumulates in the star, pp-II and pp-III branches (Table 1.1) have a higher probability of occurring and become dominant at higher temperatures ($>1.4 \times 10^7$K). As the star converts more hydrogen into helium, the core becomes denser and as a consequence, temperature and luminosity increase (path from A to B on Fig. 1.2).

It is important at this stage to explain how the energy generated in the core is transported to the surface. The photons released in the process of nucleosynthesis in the core diffuse outwards from the Sun - this is the radiative energy transfer. Radiative energy transfer is limited by the opacity of the star. Opacity tells us how likely a photon is to be absorbed by another particle to excite it and as stars are huge, dense clumps of hydrogen and other atoms, photons get absorbed or scattered. As the photons travel outward, the temperature is cooler, and in the case of the Sun, the envelope is not hot enough to ionise hydrogen, so high-energy photons get absorbed, either exciting the electron to a higher state or making it unbound resulting in H^-. Heat transfer via convection becomes more efficient than radiative transfer in the deep zone of non-ionised hydrogen. Similarly to how hot air rises, a parcel of hot hydrogen gas will rise if the surrounding is colder, and the cold gas will fall until it is heated back up. If the temperature gradient is such that as the parcel rises, the temperature of the surrounding reduces more than that of the parcel, then it will continue rising. Although eventually it will dissipate the heat and mix with the surroundings. The distance such parcel travels before mixing is called the mixing length and is given by:

$$\bar{\delta r} = \frac{1}{2}\alpha \frac{P}{dP/dr} \qquad (1)$$

where P is the pressure and α is chosen numerically so that the model fits the observations of the depth of the Sun's convection zone.

In the core the temperatures are high enough so that hydrogen stays ionised, therefore, opacity is dominated by Thomson scattering, i.e. an electron absorbing the energy of the photon is set

into a periodic motion (accelerated) and the electron re-emits the electromagnetic radiation. It takes the particle around 170,000 years to escape the radiative core of the Sun. To summarize, stars around the solar mass (0.3 $M_\odot$ - 1.5 $M_\odot$) have radiative cores and convective envelopes.

B At point B, our stellar model has now formed a helium core, shown by the green line on Fig. 1.2. When nearly all of the hydrogen is exhausted in the core, the star proceeds to burn hydrogen in the shell around the core propagating outwards, leaving the core with mostly helium. The shell burning process is more luminous because the burning moves closer to the surface, but decreases the effective temperature making the star "redder" (path from B to C on the evolutionary path). More mass is added to the core through hydrogen burning in the surrounding shell, and because the core is in the hydrostatic equilibrium with the envelope, that is the outwards radiation pressure from the core is equal to the gravitational pressure of the envelope, an increase in the mass of the core must follow an increase in radius. We know it is in hydrostatic equilibrium because otherwise, the gravity pressure from the envelope would collapse the star, or the radiation pressure from the core would repel the envelope. As the burning moves to the shell, there is no more temperature gradient in the core hence the core becomes isothermal.

C At point C and until point D the star is ascending the red giant branch (RGB). The burning continues in the shell, dumping helium into the core. Because the core is not burning and releasing energy to balance the self-gravity, it goes out of hydrostatic equilibrium and begins to contract. The density in the centre of the core gets so high that electron degenerate pressure becomes dominant over the thermal pressure of the gas: according to the Pauli exclusion principle two electrons of the same spin cannot occupy the same quantum state, and the resultant repulsion is temperature independent, allowing the core to remain in equilibrium for higher masses. The star continues to expand due to the shell burning and the increased radius is why the star is becoming brighter, while still cooling down.

D - E An interesting phenomenon happens at approximately 6.57 Gyrs, after point D. At this point, the core is almost $0.5M_\odot$ and is so dense that helium ignition occurs in the core. Helium fusion occurs via the triple-alpha process described at the end of Table 1.1. But because the degeneracy pressure is still dominating, the reaction is "contained" in the core. The temperature in the core keeps increasing, further speeding up the rate of helium fusion in a positive feedback loop called the thermal runaway. At its peak the runaway reaction produces 10^{14} times the energy of the Sun (Seeds & Backman, 2012) until thermal pressure starts to dominate again. This causes the star's luminosity to reach the brightness of a galaxy for a few seconds. This process is called a helium flash and most models cannot reproduce it. The luminosity of the helium flash is mostly contained in the star and gets absorbed by the envelope, so there is no huge spike on the modeled evolutionary path. As the star adjusts back to thermal equilibrium, the density in the central core decreases, which causes it to expand while the envelope contracts. This causes a drop in luminosity, an increase in effective

temperature (D-E on Fig. 1.2), and a significant change in the internal structure of the star (Hansen et al., 2012). The previously degenerate core becomes a convective helium-burning core and continues the triple-alpha process for another 100 Million years.

F After 100 million years, the Sun almost runs out of helium in the core and it starts climbing the asymptotic giant branch (AGB) from point E to point F. When $M_c = 0.63 M_\odot$ helium joins shell burning and the core gets hotter and denser once again, while the star swells up to about $100 R_\odot$ to maintain the equilibrium. The rapid process of helium shell burning leads to more carbon in the core, but it is not hot enough to fuse, and at the end of the asymptotic branch when $M_c = 0.92 M_\odot$ the star begins to cool down to a CO white dwarf. The evolutionary track quickly moves to the left after point F as the model skips to the white dwarf without following this process in detail. The white dwarf masses are likely overestimated because the mass-loss during the AGB phase in the stellar models is too low.

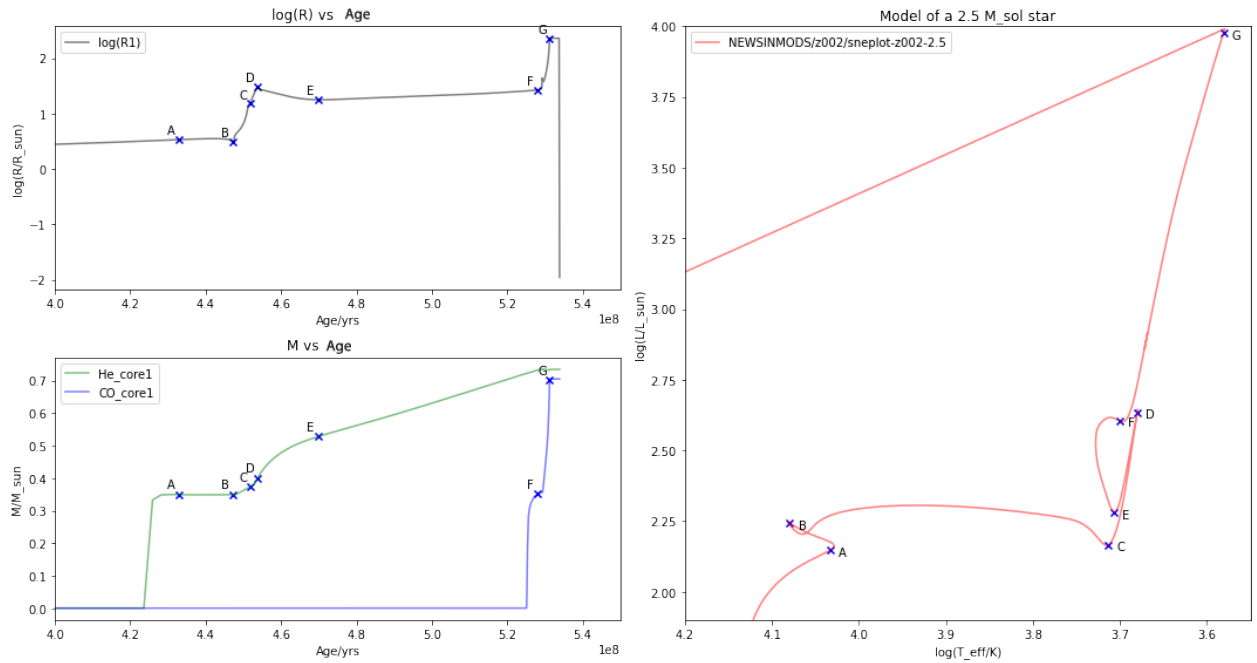### 1.1.2   Intermediate mass stars - $2.5 M_\odot$ star

Figure 1.4: Plot on the right shows the evolution of a $2.5 M_\odot$ mass star on an H-R diagram that shows Luminosity against effective temperature. Cross-points indicate important steps of evolution. Top left plot shows the radius of the star with age and bottom left plot shows the mass of the stellar core with age.
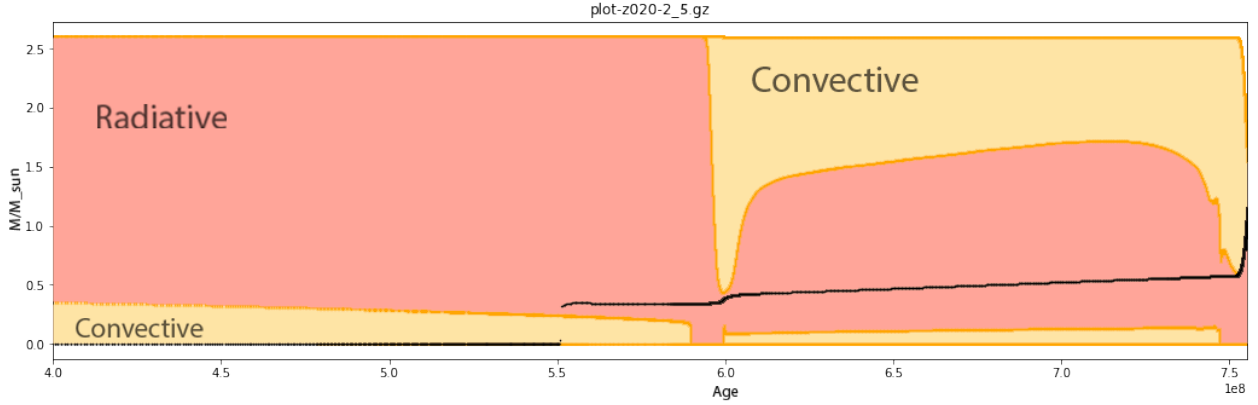
Figure 1.5: Internal structure of a $2.5 M_\odot$ star showing the radiative and convective zones. Black line indicates the helium core. Age on the x-axis is slightly different to Fig. 1.4 due to different output files used.

Next we compare the evolution of the $1 M_\odot$ star to a more massive $2.5 M_\odot$ star. A big difference in the internal structure of the $2.5 M_\odot$ star is that the core is convective, and the envelope is radiative. This is because in stars larger than $\sim 1.5 \text{M}_\odot$ the pp-chain energy generation is replaced by a more temperature-sensitive CNO cycle. The CNO cycle starts with hydrogen and carbon as a catalyst for a cyclic reaction, where carbon, nitrogen, and oxygen fuse with hydrogen to produce helium. The higher temperature gradient in the core means that convection becomes the dominant type of energy transport. As matter in the core is converted to helium the core becomes denser and contracts while the envelope is expanding. The denser core gets hotter and the star responds to this change by decreasing the effective temperature and increasing in radius to maintain the thermal equilibrium.

A This change can be seen on Fig. 1.4 as the star increases in luminosity on the main sequence. At point A most of the hydrogen in the core is exhausted and the burning moves to the shell, increasing the effective temperature as the source of energy is now closer to the surface, hence the HRD moves to the left from point A to point B. Fig. 1.5 suggests that the core at this point is only semi-convective. The black line shows how far the helium core extends and the outer part of it is radiative, most likely due to convective overshooting. Convective overshooting occurs when a "pocket" travelling through the convective layer reaches the boundary with some momentum, therefore penetrating the radiative zone and causing it to mix with the core.

B In approximately 10^5 years core mass $M_c = 0.13 M_{star}$ (the Schonberg-Chandrasekhar limit (Schönberg & Chandrasekhar, 1942)) and the gas pressure of the isothermal core cannot support the external pressure of the stellar envelope anymore. The core begins to rapidly contract, heating up until the point where helium is ignited. This process is very short (on the order of 1000 yrs) and can be observed on the H-R diagram as the Hertzsprung Gap (points B to C on Fig. 1.4. Fig. 1.11 shows an HRD with observations from an open cluster showing that it is rare to observe stars on the Hertzsprung gap). We do not see this in the $1 M_\odot$ star,

8

because for stars $<1.5M_\odot$ the core becomes degenerate before the Schonberg-Chandrasekhar limit is reached, therefore it can support the gas pressure of the envelope. As a result of the core not being degenerate, the $2.5M_\odot$ star does not experience helium flash, and helium burning is more gentle. Looking at the radius plots for this stage between points B and C, the star's radius rapidly increases due to an expanding envelope, and the star rapidly cools down. The cooling down leads to the recombination of hydrogen, so it is not ionised anymore. The solar mass example describes how this affects opacity, and the rapid cooling means that the star's outer envelope becomes convective.

C When the star becomes fully convective, it reaches point C, or the Hayashi limit, which is a numerical limit on how big a fully convective star can get for a certain mass in the models. It is a limit to how far to the right the star can go on the HR diagram, which is why after point C the star follows an almost vertical line (Hayashi & Hoshi, 1961). The prior rapid cooling made the star's equilibrium unstable, so as it stabilises the convective envelope retracts a little bit, mixing in the radiative matter of the core.

D - E - F After this stage the star joins the RGB. Hydrogen continues to burn in the shell driving the compression of the helium core further and increasing the temperature and luminosity. The core contracts until it is hot enough to ignite helium via the triple-alpha process, which occurs at point D and sends the star into a "Blue Loop" (D→E→F). At point F, helium in the centre is almost exhausted and helium burning also moves to the shell, leaving a carbon core $M_c = 0.3M_\odot$. The luminosity rapidly increases as the double-shell burning heats up the core and the star expands to maintain the thermal equilibrium.

G Point G and onwards is the end of the life of the star. It has grown so big that the outer parts of the envelope are very weakly bound and get stripped via stellar winds. The envelope is being further stripped in thermal pulses and the luminosity decreases. Thermal pulses result from thermonuclear runaway from the helium shell into the envelope and quickly grow in strength (Gallino et al., 1998). Eventually, the core and the burning shells are exposed, and the star cools down to become a CO white dwarf.

Fig. 1.6 shows a 4.5 $M_\odot$ star and the evolution process is very similar to that of a 2.5 $M_\odot$ star, however the timescale is shorter. Heavier stars exert more pressure on the core, and as a result, the rate of fusion is higher. The lifetime of a 2.5 $M_\odot$ star is approximately four times longer before it burns through all of its fuel to become a CO white dwarf.
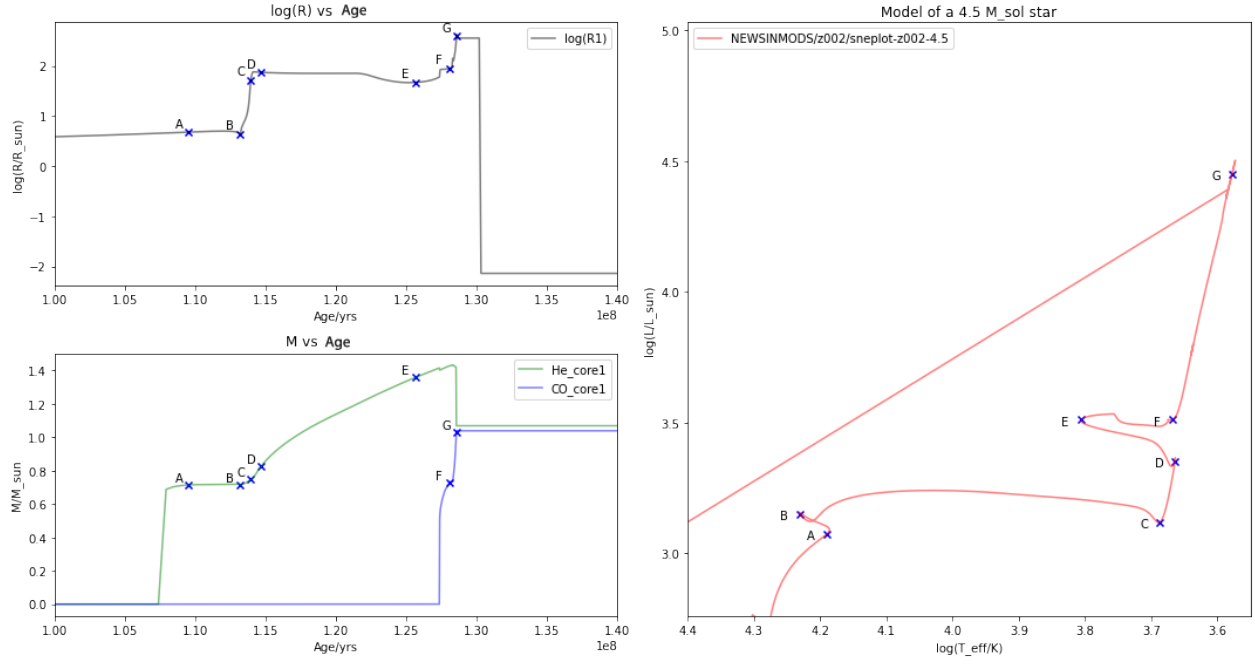
Figure 1.6: Plot on the right shows the evolution of a $4.5M_\odot$ mass star on an H-R diagram that shows Luminosity against effective temperature. Cross-points indicate important steps of evolution. Top left plot shows the radius of the star with age and bottom left plot shows the mass of the stellar core with age.
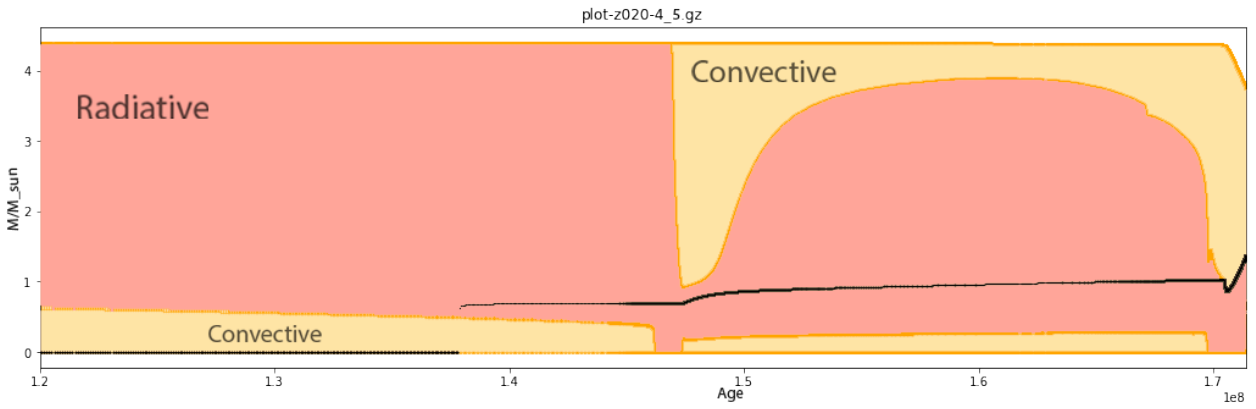
Figure 1.7: Internal structure of a $4.5M_\odot$ star showing the radiative and convective zones. Black line indicates the helium core. Age on the x-axis is slightly different to Fig. 1.6 due to different output files used.

10

1.1.3 High mass stars - $10 M_\odot$ star
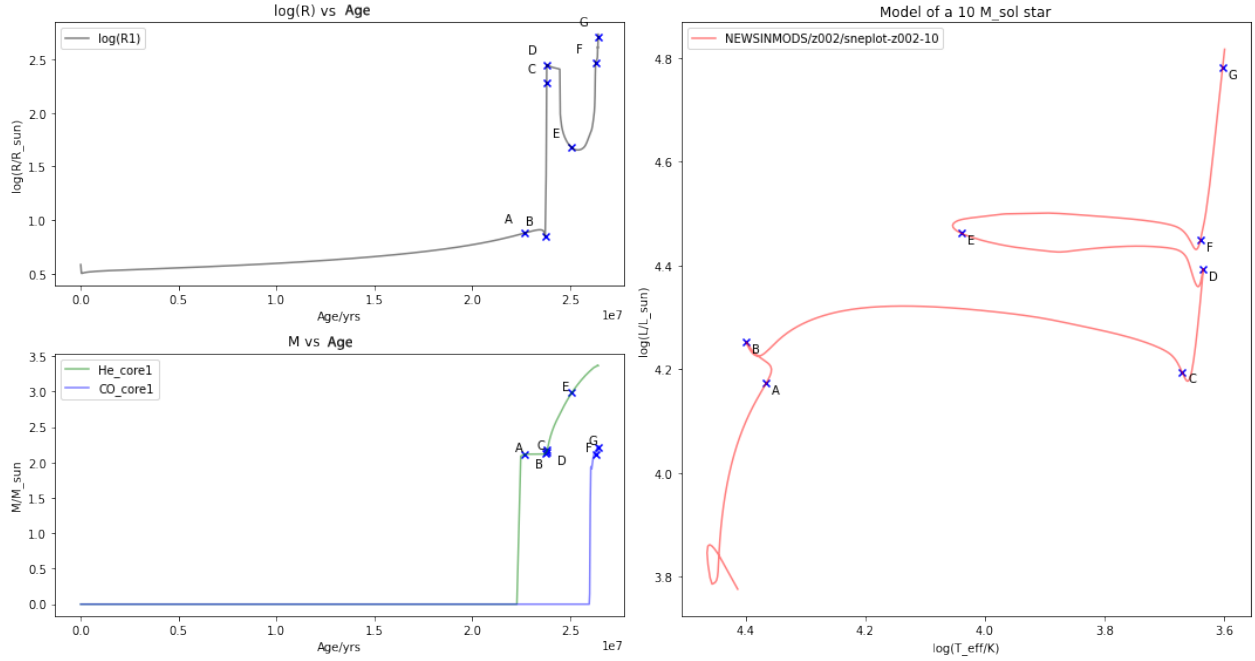
Figure 1.8: Plot on the right shows the evolution of a $10 M_\odot$ mass star on an H-R diagram that shows Luminosity against effective temperature. Cross-points indicate important steps of evolution. Top left plot shows the radius of the star with age and bottom left plot shows the mass of the stellar core with age.
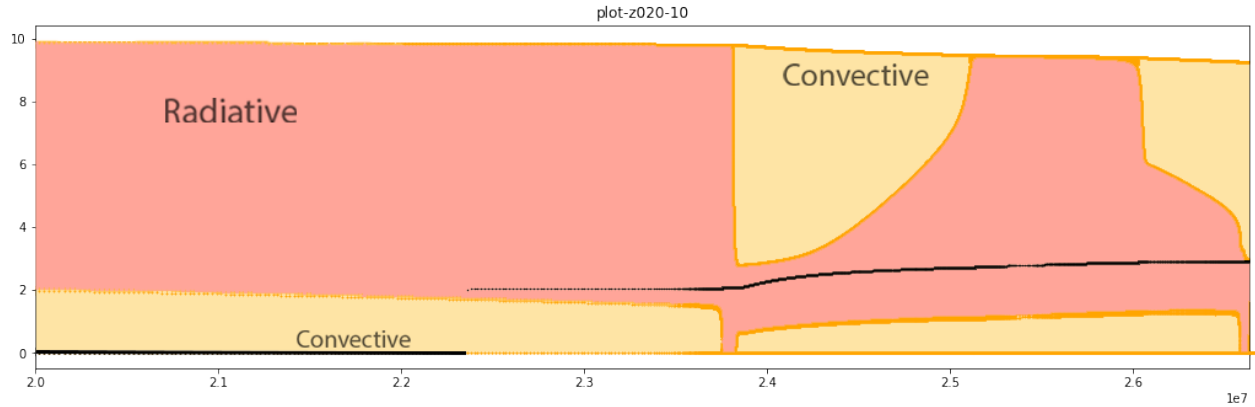
Figure 1.9: Internal structure of a $10 M_\odot$ star showing the radiative and convective zones. Black line indicates the helium core. Age on the x-axis is slightly different to Fig. 1.8 due to different output files used.

Apart from the difference in time scales and core mass, high mass stars follow a similar evolutionary path as intermediate mass stars in the early stages. The difference comes in past carbon ignition as the additional mass allows for the fusion of heavier elements. Carbon fuses into oxygen, and then neon for a 10 $M_\odot$ star, and in heavier stars it proceeds with burning to magnesium and silicon and finally an iron core. The timescale for heavier elements is much shorter, where the burning of most of the carbon to neon lasts approximately 1000 years.

The evolution of high mass stars is outlined below:

A) Core hydrogen is exhausted and burning moves to the shell.

B) Schonberg-Chandrasekhar limit is reached and the core begins to contract - Hertzsprung gap.

C) Hayashi Limit is reached. Deep convective envelope develops. Core helium ignition.

D) Core helium burning. Star goes onto the "Blue Loop".

E) Helium is nearly exhausted in the core and the burning moves to the shell.

F) Carbon ignition starts.

G) Fusion of neon and further elements begins.

Fig. 1.8 shows that the mass of the remnant core is approximately $2\ M_\odot$ which is above the Chandrasekhar limit ($1.4M_\odot$). This is the limit that electron degeneracy pressure is able to support, so rather than becoming a white dwarf, the remnant core collapses to a neutron star. A neutron star is a few tens of kilometres in diameter as it is a super dense ball of neutrons.

ENERGY GENERATION REACTION	ENERGY OUTPUT
$H + H + e^- = D + \nu_e$	(1.4 MeV)
$H + D = {}^3He + \gamma$	(5.49 MeV)

<div align="center">PP-I</div>

${}^3He + {}^3He = {}^4He + 2\,H$	(12.86 MeV)

<div align="center">PP-II</div>

${}^3H + {}^4H = {}^7Be + \gamma$	(1.59 MeV)
${}^7Be + e^- = {}^7Li + \nu_e$	(0.86 MeV)
${}^7Li + {}^1H = {}^4He + 2\;{}^4He$	(17.35 MeV)

<div align="center">PP-III</div>

${}^7Be + {}^1H^- = {}^8B + \gamma$	(1.59 MeV)
${}^8B = {}^8Be + e^+ + \nu_e$	(10.78 MeV)
${}^8B = 2\,{}^4He$	

<div align="center">CN Cycle</div>

${}^1H + {}^{12}C^- = {}^{13}N + \gamma$	(1.95 MeV)
${}^{13}N = {}^{13}C + e^+ + \nu_e$	(1.2 MeV)
${}^{13}C + {}^1H = {}^{14}N + \gamma$	(7.54 MeV)
${}^1H + {}^{14}N = {}^{15}O + \gamma$	(7.35 MeV)
${}^{15}O = {}^{15}N + e^+ + \nu_e$	(1.73 MeV)
${}^1H + {}^{15}N = {}^{12}C + {}^4He + \gamma$	(4.96 MeV)

<div align="center">NO Cycle</div>

${}^1H + {}^{15}N^- = {}^{16}O + \gamma$	(12.13 MeV)
${}^1H + {}^{16}O = {}^{17}F + \gamma$	(0.6 MeV)
${}^{17}F = {}^{17}O + e^+ + \nu_e$	(2.76 MeV)
${}^1H + {}^{17}O = {}^{14}N + {}^4He$	(1.19 MeV)

<div align="center">*triple* $-\alpha$</div>

${}^4He + {}^4He^- = {}^8Be$	(-0.09 MeV)
${}^8Be + {}^4He = {}^{12}C$	(7.37 MeV)

Table 1.1: Main energy generation reactions for low and intermediate mass stars (Eldridge & Tout, 2019; Krane et al., 1988)

1.2 Star Clusters and Blue Stragglers

But how do we confirm that our models are correct and compare different stars, whose lifetimes are over millions of years where we simply would not be able to observe any star for this long? The solution is to use star clusters. As discussed earlier, stars in a star cluster have all formed from the same cloud of gas and around the same time. This means that we can observe where real stars of different masses lie on the HR diagram and compare that with theoretical models. With so many observations we have now developed quite accurate predictions for the temperature-luminosity relations based on mass, which made it possible to estimate the age and distance to star clusters using theoretical models. However there is still a lot of information we can study using star clusters. For example, formation of more unique stars, that do not fall under the descriptions we have covered above.

The evolution process discussed in Section 1.1 explains how main sequence stars, red giants and white dwarfs are formed in the cluster, but does not explain the formation of some of the observed stars in this mass range. This takes us back to the Algol paradox resolution first proposed by Crawford (1955) who suggested that mass must have been transferred from one star to another, resulting in a larger and brighter main sequence star.

Fig. 1.10 shows a colour magnitude diagram of the M67 cluster. A colour magnitude diagram is analogous to the HR diagram, but instead of Luminosity and temperature it shows the brightness magnitude of the star in a particular photometric filter on the y-axis, and the colour as the difference in two photometric bands on the x-axis. They are generally used instead of H-R diagrams by observers, as photometric data for stars is more available. When the colour and magnitude of all stars in a given cluster are plotted on a CMD the path they follow is indicative of the age of the cluster. Single star evolution predicts that they will fall along a line of constant age called an isochrone. Fig. 1.11 shows a modeled distribution of single stars at a constant age, similar to an isochrone but with contours that show the number of stars lying in that region. If there were no binary interactions, we could expect all stars to be on those contours, but the overlaid observations show there are stars above the Hertzsprung gap. Stars that are more luminous than the typical population are called "stragglers", as they should not be alive but are "straggling" behind the age of the whole cluster. Blue straggler stars (BSSs) are the most long-lived stragglers, and are therefore best for studying the formation of these unique stars. The best explanations we have for their existence is that they are a result of binary stars interacting (Knigge et al., 2009).
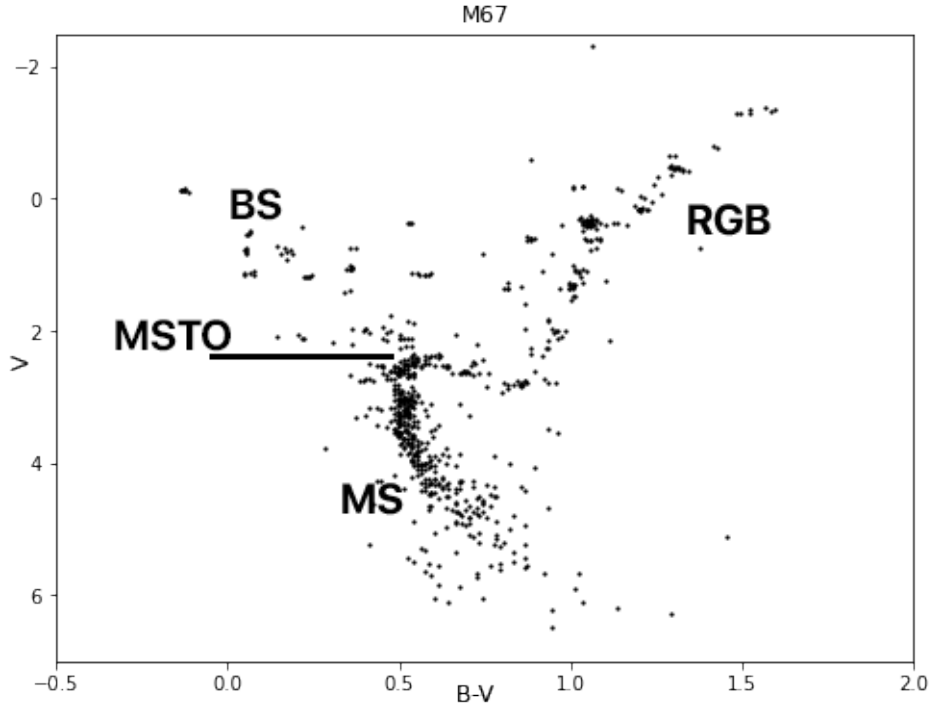
Figure 1.10: Colour-Magnitude Diagram of an old open cluster M67. Observational data obtained from the WEBDA catalogue.
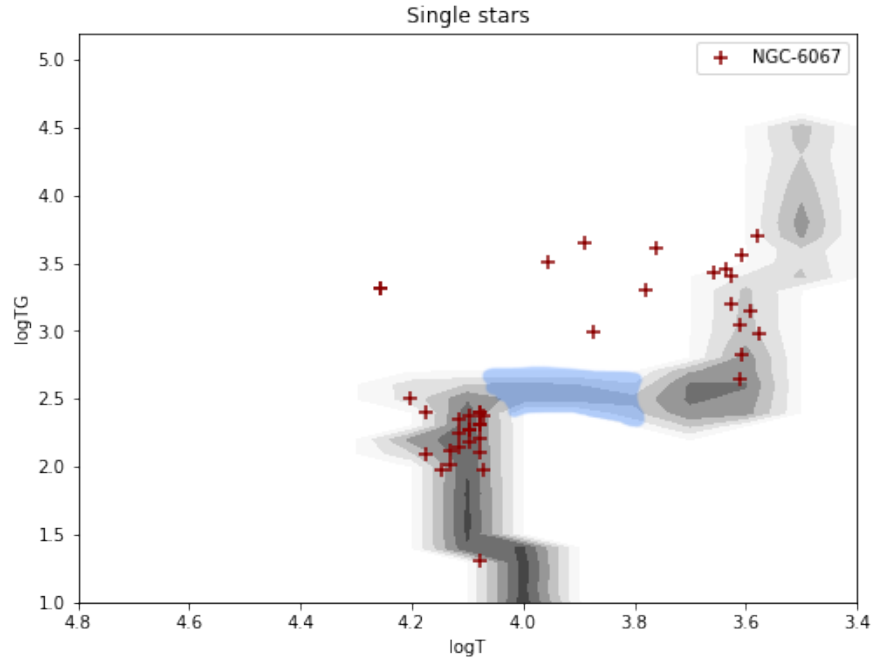
Figure 1.11: H-R diagram with temperature and surface gravity data from NGC-6067. An H-R diagram shows the relation between the temperature (x-axis) and luminosity (y-axis, here log(TG) is plotted as $L \propto \log(T^4/g)$). Main sequence is in the 4.2-4 logT range, red giant branch lies between 3.8-3.4 logT. Blue region shows the H-R gap. It is lighter than MS and RGB, as it is rare to see stars in this region due to the short time they spend there. HRD generated using `hoki` (Stevance et al., 2020a).

Sandage (1953) discovered BSSs while mapping the stars of the M3 cluster onto the CMD. He noticed that they stand out from typical single stars as they are brighter and bluer than main sequence turnoff stars. Main sequence turnoff (MSTO) is the point where main sequence stars start evolving to red giants turning Red on the colour magnitude diagram. As a consequence, blue stragglers appear younger than the rest of the cluster, as stars this bright are normally cool. Blue stragglers seem to have "extra fuel" compared to other stars in the cluster and are often called "Rejuvenated". Details of the physics behind the formation of BSSs and what systems lead to these stars are still uncertain, as most of the literature explores into an enhanced mass loss of a donor, rather than the mass gain of a secondary, which is what drives the BSS. This is most likely because detailed models are very difficult and most models track only the primary star in detail. The goal of this thesis is to research the physics behind how these stars are produced and the details of the binary systems that are involved in the process.

Multiple formation methods of BSSs have been proposed, with a possibility of different mechanisms of formation dominating depending on the cluster type (open or globular). The concensus is that they either form from a merger (Hurley et al., 2005) or through mass transfer via Roche Lobe Overflow in a binary system (first proposed by McCrea (1964)). Most likely, both of these methods account for the total population of blue stragglers in clusters, however mergers are unlikely to have a significant contribution in open clusters, where the cluster density is too low (Press & Teukolsky, 1977). In addition, most open clusters survive on average a few hundred million years, and observations show that clusters with most blue stragglers are older than 1.5 billion years (Leiner & Geller, 2021; Jadhav & Subramaniam, 2021).

Mass transfer from the donor to the accretor can lead to the rejuvenation of the latter, making it appear younger than it actually is and if the accretor is a near MSTO star, the system will evolve into a white dwarf and a blue straggler pair. Understanding of this mass transfer process is important for our understanding of the formation of other low-mass binary products such as Type Ia supernovae and white dwarf systems (Leiner & Geller, 2021). Type Ia supernovae are the result of an explosion of a CO white dwarf when it exceeds $1.4M_\odot$ and they are essential to nucleosynthesis, so they are responsible for a large percentage of elements past oxygen on the periodic table in the Universe. Multiple studies have shown the dependence of the number of blue stragglers with age, with the fractional number of BSSs increasing from log(age)=9, a decrease around log(age)= 9.5-9.7 (depending on the study) and consequent increase at the oldest ages. In this study we use models from BPASS to accurately recreate the ratio of blue stragglers to red giants in the population at log(age) 9-10 collected by (Leiner & Geller, 2021), and we explore the physics beyond what helps the models achieve results that are more accurate than previous studies.

1.3   Mass Transfer and Roche-Lobe

Many stars interact in their lifetime. The ratio of interacting binaries was estimated to be 70% in O-type main sequence stars (from a sample of galactic open clusters (Sana et al., 2012)), which means that to accurately represent stellar populations with population synthesis, we need to account for the interactions between the stars. The way stars interact is through mass transfer. One of the stars expands during its evolution and eventually fills a region at which the mass on the surface is not tightly bound to the star and will transfer to the nearby secondary star. The region at which mass is still bound to the star is defined as the Roche-Lobe (Fig. 1.12). There are many aspects to mass transfer: the timescales of mass transferring onto the secondary, how effective the transfer is, and how both stars react to mass transfer.

Roche-Lobe overflow is the main way matter is exchanged in a binary. Roche-Lobe surface is defined by the gravitational potential of the binary in a rotating frame of reference, which allows to ignore the Coriolis forces. The equipotential surfaces around each star are approximately spherical, elongated in between the shortest point between the stars. The points where the gravitational forces are equal are called the Lagrangian points, and are shown on Fig. 1.12. L1 is the point of minimum equipotential, and if the star fills its Roche-Lobe, the mass transfer will flow through this point.
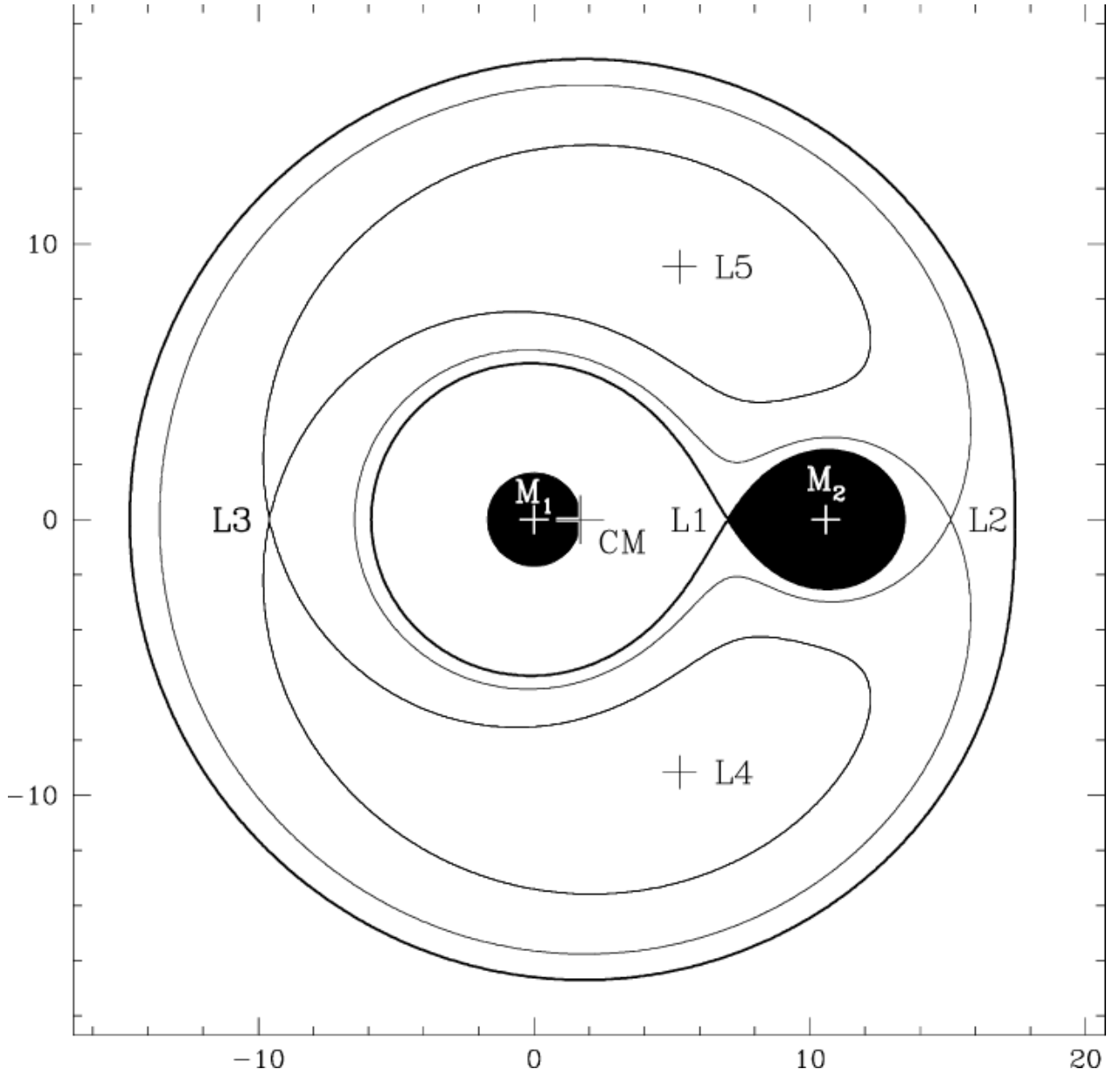
Figure 1.12: Schematic view of the system in the equatorial plane (coordinates in R_{sol}). Solid lines represent equipotential lines and Lagrange points are labeled. The secondary star (M2) fills its Roche-Lobe. Fabio et al. (1998)

The radius of the Roche-Lobe has been fitted by Eggleton (1983) and is accurate to 1%.

$$R_{L1} = \frac{0.49 q_1^{2/3} a}{0.6 q_1^{2/3} + \ln(1 + q_1^{1/3})} \qquad (2)$$

where $q_1 = M_1/M_2$ and a is the separation between two stars.

It assumes that the orbits are circularised and the spins are synchronised, which is in general true and is achieved by the tidal friction in the binary. Circularisation of the orbit may occur before tidal synchronisation in the case of mass transfer via stellar winds. (Hurley et al., 2002a).

The stability of the mass transfer depends on the response of the radius of the donor star to the mass loss, i.e. if a star shrinks on mass loss then the mass transfer is stable, if it grows, further filling Roche-Lobe, then the mass transfer is unstable. In binary systems where the total mass and angular momentum are conserved, this is given by Eq. 3.

$$\zeta_L = \left(\frac{\delta \log R_{L1}}{\delta \log M_1} \right)_{M,J} \tag{3}$$

where ζ_L describes the rate of change of the Roche-Lobe radius R_{L1} of the donor to the change in mass M_1. This can be approximated by $\zeta_L = 2.13q - 1.67$ ($q = M1/M2$). If ζ_L is positive (q>0.78), then the Roche-Lobe radius of the donor decreases as mass is transferred (alternatively, if $\zeta_L < 0$, then R_{L1} expands in response to mass transfer). This describes the response of the Roche-Lobe to mass transfer, now we need to know the response of the star. There are two stability equations, one is for the immediate, adiabatic response of the star (Eq. 4) and the other is for when the star regains thermal equilibrium (Eq. 5). (X_i) is the chemical composition of the donor and is assumed to be constant.

$$\zeta_{ad} = \left(\frac{\delta \log R_{L1}}{\delta \log M_1} \right)_{S,\{X_i\}} \tag{4}$$

$$\zeta_{eq} = \left(\frac{\delta \log R_{L1}}{\delta \log M_1} \right)_{\{X_i\}} \tag{5}$$

If $\zeta_L > \zeta_{ad}$ then the Roche-Lobe radius shrinks faster than the radius of the star, leading to a positive feedback loop as more and more mass is transferred onto the second star. The mass is transferred on a dynamical timescale (on the order of tens of years), however the secondary in general cannot accrete the mass this fast. The result of this unstable mass transfer is a formation of a common envelope (CE), where the non-accreted material from the donor envelopes the second star as illustrated on Fig. 1.13.

If $\zeta_L < \zeta_{ad}$ and $\zeta_L > \zeta eq$ the donor shrinks, and then expands on the thermal timescale. The mass transfer in this case occurs on a thermal timescale (10^6 yrs).

If $\zeta_L < \zeta_{ad}$ and $\zeta_L < \zeta eq$, then after the initial decrease of the donor's radius mass transfer stops, until the star fills the Roche-Lobe again through the nuclear evolution. Hence mass transfer occurs on the nuclear timescale (10^9 yrs). (Eldridge & Tout, 2019)

The effect of this conservative mass transfer on the separation of the binary is positive, meaning separation increases, if $M_2 > M_1$, and negative if $M_1 > M_2$ (Eq. 7). We see in the results section that as mass transfer is happening, the ratio of masses can flip, causing mass transfer to go from unstable to stable.

$$\frac{\dot{a}}{a} = 2\frac{\dot{M_1}}{M1} \left(\frac{M_1 - M_2}{M_2} \right) \tag{6}$$

19

If the total mass is not conserved however, which is often the case, then the separation will change. Equation 7 tells us, under assumption of conserved angular momentum, that if we have mass transfer from M1, i.e $\dot{M_1}$ is negative, then $\frac{\dot{a}}{a}$ is positive and therefore the orbit will widen. This will have a positive effect on the change in Roche-Lobe radius.

$$\frac{\dot{a}}{a} = -\frac{\dot{M_1}}{M1}\left(\frac{M_1 + 2M_2}{M_1 + M_2}\right) \tag{7}$$

If the mass transfer occurs during core hydrogen burning of the donor, typically on the main sequence, then the mass transfer tends to be stable and is classified as Case A. Case B mass transfer occurs post-hydrogen core burning, when the donor is on the giant branch, and is generally unstable as the convective envelope expands upon mass loss. If the mass transfer first occurs in the post-helium burning stage of the evolution, then mass transfer is unstable and non-conservative and will lead to a common envelope. This is Case C mass transfer. (Lamers & M. Levesque, 2017).
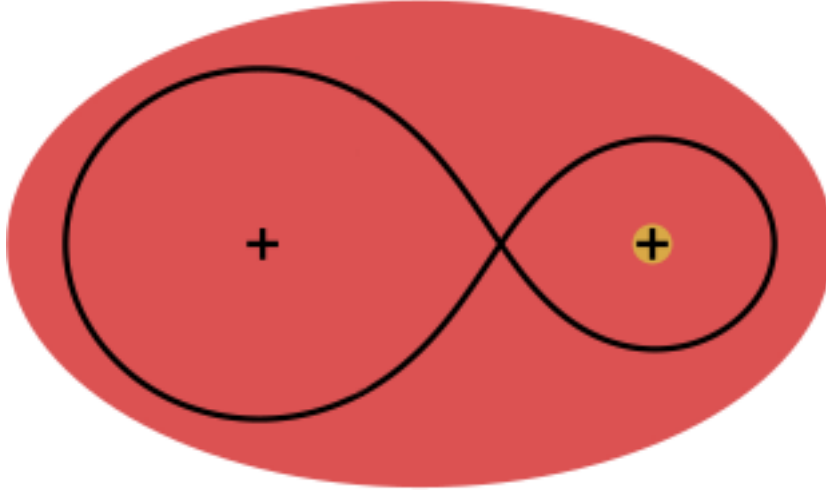
Figure 1.13: Common Envelope. Image from Izzard et al. (2011)

1.4   Previous Research

If blue stragglers form via binary interaction, then they are a sensitive test for the physics of binary interaction. This chapter summarises some of the latest studies that have used blue straggler observations to test against current binary computational models.

M67 is one of the best studied clusters, and there have been a few studies modelling the blue straggler population. Hurley et al. (2005) used both cluster dynamics and binary mass transfer in their N-body model and the resulting simulation had 20 BSSs (while the observations show 28). They point out that cluster dynamics played an important role in the formation of BSSs even for those formed via mass transfer in a binary, and only seven of them evolved in isolated binaries.

While many studies look at clusters in isolation to determine the physics behind the blue straggler formation, a few studies examine and compare multiple clusters of different ages.

Leiner & Geller (2021) present their results showing the ratio of BSSs to red giants in 16 open clusters with ages ranging from log(age)=9.15 to log(age)=10.0 for different mass transfer stability criteria. They filter the observational data using Gaussian fits to proper motion to determine whether each member is part of the cluster, and then calculate the number of blue stragglers and red giants for 16 open clusters using the Gaia Dr2 database. Their results are reported in Table 2.2. For the comparison with the observational data they used COSMIC population synthesis code.

COSMIC (Breivik et al., 2020) is a binary population synthesis code, designed to simulate compact-object binary populations and their progenitors. Leiner & Geller (2021) used a rapid stellar formation history to create a population of 100,000 binaries, meaning that all stars are created at the same time. Because the population is exclusively binary, which is not realistic for the red giant stars, they multiply the number of RGB stars by a factor of four based on the observed percentage of spectroscopic binaries in open clusters for the similar period domain, which is 25% (Geller et al., 2009; Milliman et al., 2014). In their study they use binary parameters from Moe & Di Stefano (2017), which record twin fractions (where q=M1/M2 >= 0.95) from $F_{twin} = 0.30$ for $M_1 = 0.8 - 1.2\ M_\odot$ and $log(P/days) = 1$ to $F_{twin} = 0.10$ for $M_1 = 2 - 5\ M_\odot$ and $log(P/days) = 3$. These are the mass ranges we find in systems with blue stragglers (Jadhav & Subramaniam, 2021). In their models they use Bondi-Hoyle wind accretion with the default value of $\alpha_w = 1.5$ and mass-loss rate due to winds is lowered from the default value of $\eta = 0.5$ to $\eta = 0.1$ based on the observations of asteroseismic measurements of RGB mass loss in older open clusters (Miglio et al., 2011). It is important to note that multiplying the number of red giants by four is not a good approach. 25% is the number of spectroscopic binaries recorded, however binary interactions may occur in the life of a star and later the donor and accreter may separate. So we suspect the ratio of blue stragglers to red giants has been artificially decreased due to this crude approximation, hence why N_{BSS}/N_{RGB} is below 0.05 for the Hurley et al. (2002b) stability criteria. BPASS mass transfer is also based upon Hurley et al. (2002b), but the ratio of blue stragglers is much larger. But removing the factor of four would not make the models fit observations. We explain later that the difference most likely arises from COSMIC using approximations for mass-loss and not reflecting the changes on the stellar model as it is done in BPASS.

They test four stability criteria which all yield different results because of how they treat mass transfer: Hurley et al. (2002b), Hjellming & Webbink (1987), non-conservative version of Hjellming & Webbink (1987), L2/L3 Overflow by Woods & Ivanova (2011), and in addition they test a case where RGB donors always have stable mass transfer. For the latter they set $q_{crit} = 100$ in COSMIC for the giant stars. This tests how many blue stragglers can be created if all low mass red giant binaries that interact produce blue stragglers. What they found is that only non-conservative criterion has good predictions at ages below 2 Gyrs (log(age)<9.3) but it significantly underpredicts the ratio of BSS/RGB at older ages. L2/L3 Overflow predictions are within the error bars for <2

Gyrs, but do somewhat better at older ages, however still significantly underpredicting the ratio. The other two criteria completely underpredict all observations, while the No CE approach overpredicts at ages before 3 Gyr (log(age) = 9.5) and underpredicts at the later ages.

Jadhav & Subramaniam (2021) support Leiner & Geller (2021) observations regarding the age distribution of BSSs, particularly those that formed via mass-transfer, but they have extended their observations to 228 clusters (including globular clusters). They suggest that at least 54% of the BSSs have formed through the binary mass transfer route.

Another study by Boffin, H. M. J. et al. (2014) used a PIONEER interferometer to detect six low-mass red giants, three of which have a Roche-Lobe filling factor close to one. These are very good candidates for the BSS donors as they are in the right mass range. The study provides a lot of details on the parameters of the stars, so we are able to compare these stars with similar BPASS models.

1.5   Thesis Outline

In section 2 we introduce the binary evolution code used to create the models studied in this thesis, as well as observations that we compare against, and tools and methods we use to make the comparison. Section 3 presents our results of estimating BSS populations and compares them to other models. We then proceed to look at the details of binary evolution and how detailed binary models handle mass transfer. The last chapter summarises the results, implications and possible future work.

2 Observations and Computation Methods

2.1 Leiner & Geller (2021) Observations

In this thesis, we compare the results of BPASS models to the observational data from Leiner & Geller (2021) (Table 2.2), where they provide observations for 16 open clusters. Clusters were selected such that the cluster's total mass is $M_{TOT} > 200 M_{\odot}$, distances < 3.5kpc and ages > 1 Gyr as this provides clusters with many members and cleaner data. Cluster members are obtained using the Gaia Dr2 catalogue, where they select members 0.1 arcmin from the cluster centre to determine the cluster proper motions. Then a Gaussian is fit to the proper motions of all members from a higher solid angle, determining the membership by dividing the value of the cluster Gaussian by the sum of the cluster and field Gaussians at the proper motion of that source. The distance to the cluster is obtained by fitting a Gaussian to the distances to each member and selecting the mean of the Gaussian (Leiner & Geller (2021), Section 2.2. No details on the range of the Gaussian distribution provided). Note that Gaia does not provide distances for the sources, and due to the nature of the Gaia recorded parallax, they do not recommend using the standard method of obtaining the distance to the cluster as an inverse of the parallax r=1/ω. Instead, they suggest to follow the Bayesian approach, with a posterior given as

$$P(r|\bar{\omega}) = \frac{1}{Z} P(\bar{\omega}|r) P(r) \tag{8}$$

With the following prior:

$$P(r) = \begin{cases} \frac{1}{2L^3} r^2 e^{-r/L}, & \text{if } r > 0 \\ 0, & \text{otherwise} \end{cases} \tag{9}$$

They identify BSSs as stars that are bluer and are brighter than one magnitude below MSTO, and red giants as stars redder and brighter then the end of Hertzsprung Gap (see RGB on Fig. 1.10). Table 2.2 shows the recorded BSS numbers and RGB numbers for each cluster, and Fig. 2.14 shows their ratios plotted against age and overlaid on top of the results of the modeled results. While different stability criteria agree with observations at particular ages, e.g. non-conservative mass transfer predicts N_{BSS}/N_{RGB} accurately at approximately 1.5 Gyrs, but decreases after that, while the observed ratio continues to grow.

BSS Gaia DR2

Cluster	Distance (pc)	[Fe/H]	Age	$E(bp-rp)$	r_{hm} (pc)	r (pc)	N_{BSS}	N_{YSS}	N_{RGB}
NGC 752	440 ± 20	0.0	1.4 Gyr	0.04	4.2	16	1	0	15
NGC 7789	2080 ± 190	0.0	1.4 Gyr	0.38	6.4	20	10	0	165
Collinder 110	2200 ± 300	0.0	1.6 Gyr	0.50	5.4	20	8	0	74
NGC 6939	1850 ± 140	0.0	1.6 Gyr	0.44	2.3	16	4	0	44
IC 4651	920 ± 50	0.0	1.8 Gyr	0.18	1.7	8	4	1	24
NGC 2506	2900 ± 500	−0.25	2.0 Gyr	0.08	5.0	16	9	0	72
NGC 6819	2600 ± 400	+0.25	2.5 Gyr	0.10	2.4	16	17	0	76
Ruprecht 147	300 ± 10	0.0	2.8 Gyr	0.08	2.2	8	3	0	10
Ruprecht 171	1530 ± 150	+0.4	2.8 Gyr	0.26	1.8	8	5	0	33
NGC 6253	1670 ± 160	+0.4	3.2 Gyr	0.28	1.6	8	16	1	55
Berkeley 98	3400 ± 160	0.0	3.5 Gyr	0.22	2.3	8	5	1	21
M67	840 ± 60	0.0	4.0 Gyr	0.05	2.5	12	16	0	43
NGC 2243	3500 ± 700	−0.5	4.5 Gyr	0.06	2.6	12	14	0	34
NGC 188	1830 ± 170	0.0	6.3 Gyr	0.12	4.6	16	16	0	60
Berkeley 39	3200 ± 800	−0.25	8.0 Gyr	0.10	2.1	12	24	4	70
Berkeley 17	2800 ± 750	−0.25	10 Gyr	0.62	2.7	12	20	2	59

Table 2.2: Observational data for 16 open clusters of ages 1.4-10 Gyrs. Table 1 from Leiner & Geller (2021)
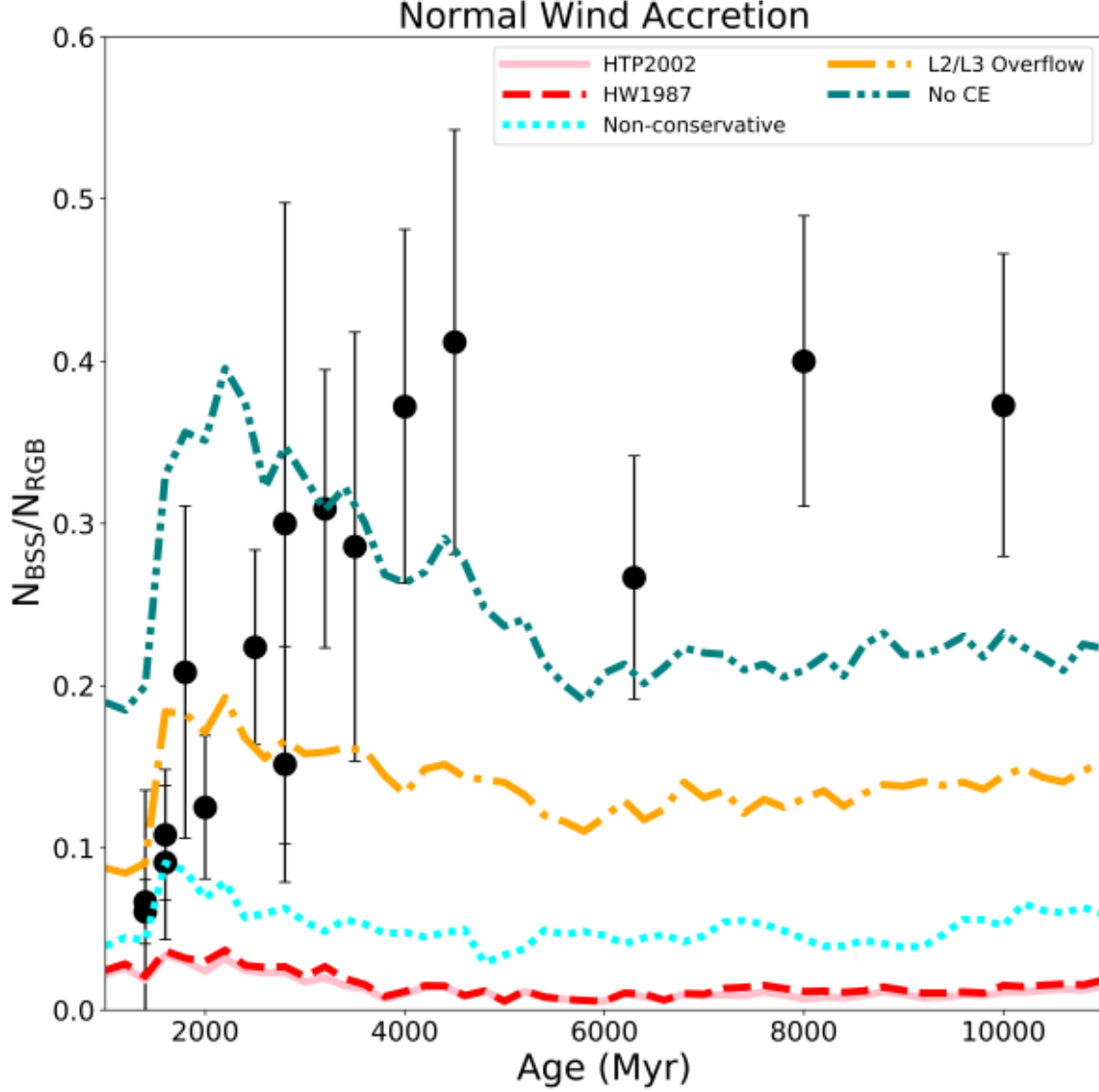
Figure 2.14: Observed ratio of BSSs to the number of RGB stars in open clusters (black points) compared to COSMIC population synthesis models with stability criteria discussed in Section 1.7 (coloured lines). Figure is taken from Leiner & Geller (2021) to display their results.

2.2 Jadhav & Subramaniam (2021) Observations

Jadhav & Subramaniam (2021) is an observational study in which the authors released their observations on 670 open clusters using the Gaia Dr2. Catalogue, with over 800 BSSs spanning ages log(age)=8.5 to log(age)=10, with the cut-off criteria on the CMD selected manually. They separate the recorded BSSs into three categories, based on the mass transfer efficiency value (Eq. 10) in the case where both accretor and the progenitor were MSTO stars, and find that most mass transfer BSSs fall under $M_e < 0.5$. Table 2.3 shows their data binned by log(age).

Binning type		No. of Clusters	No. of BSSs	No. of BSSs in $\mathcal{M}_e$ classes		
				low	high	extreme
log(age)	8.50–9.00	56	90	43	27	20
	9.00–9.25	77	234	109	71	54
	9.25–9.50	65	247	121	84	42
	9.50–9.75	24	190	123	49	18
	9.75–10.0	6	107	75	29	3
log(cl_mass)	2.0–3.0	55	85	44	28	13
	3.0–3.5	88	207	112	61	34
	3.5–4.0	60	272	140	83	49
	4.0–4.5	21	193	101	56	36
	4.5–5.0	4	111	74	32	5
Total		228	868	471	260	137

Table 2.3: BSS observations from over 200 old open clusters summarised. The first column shows the limits of cluster age and mass for each bin. The second and third columns have the number of clusters and BSSs in the respective bins. M_e shows mass transfer efficiency, where low M_e corresponds to BSSs formed via mass transfer. Table 1 from Jadhav & Subramaniam (2021)

$$M_e = \frac{M_{BSS} - M_{MSTO}}{M_{MSTO}} \tag{10}$$

where M_{BSS} is the blue straggler mass, and M_{MSTO} is the mass of the main sequence turnoff, which occurs at the top of the main sequence. Fig. 2.16 indicates that BSSs with $M_e < 0.5$, which increase with time, have a different trend to those with $M_e > 0.5$. This means that their formation methods are different. Jadhav & Subramaniam (2021) suggest that majority of stars with $M_e > 0.5$ belong to the merger formation channel as their mass transfer seems to be non-conservative. This explains the decline of $M_e > 1$ after log(age/yr)=9 as stars start dying and there is less possibility for merger systems. Therefore $M_e < 0.5$ must be forming via stable mass transfer.
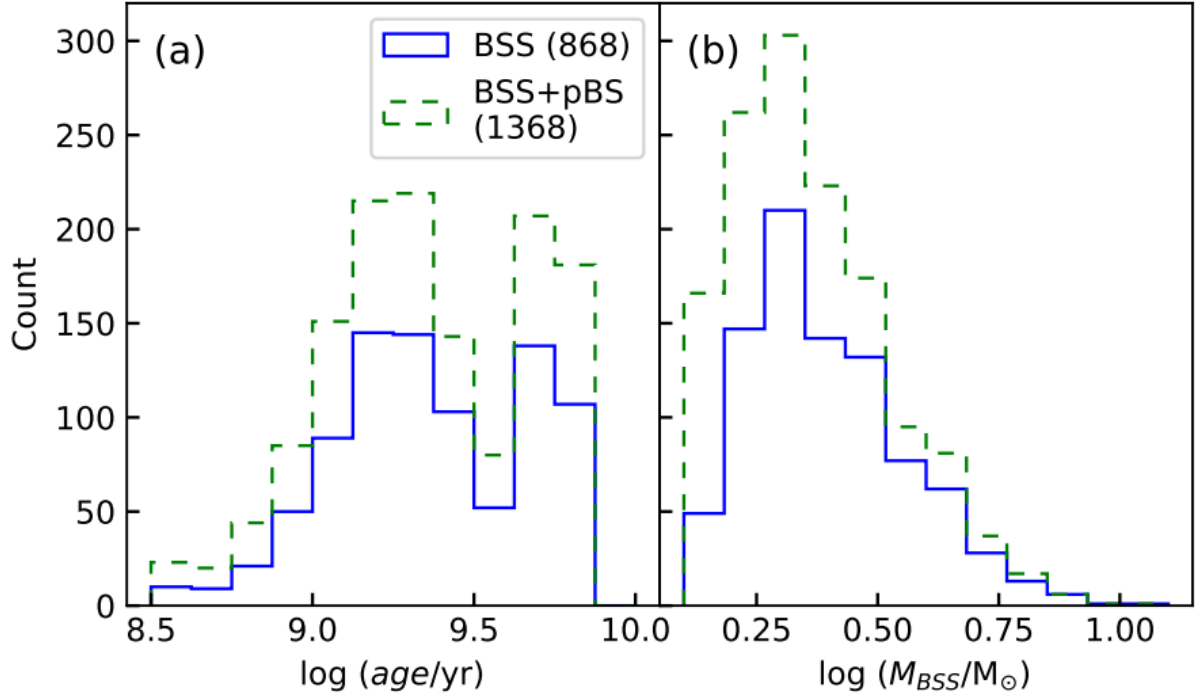
Figure 2.15: Left: Number of BSSs with age. Blue line represents the number of BSSs, green line includes possible BSSs. Right: Distribution of age of all BSSs. Fig.2 from Jadhav & Subramaniam (2021)
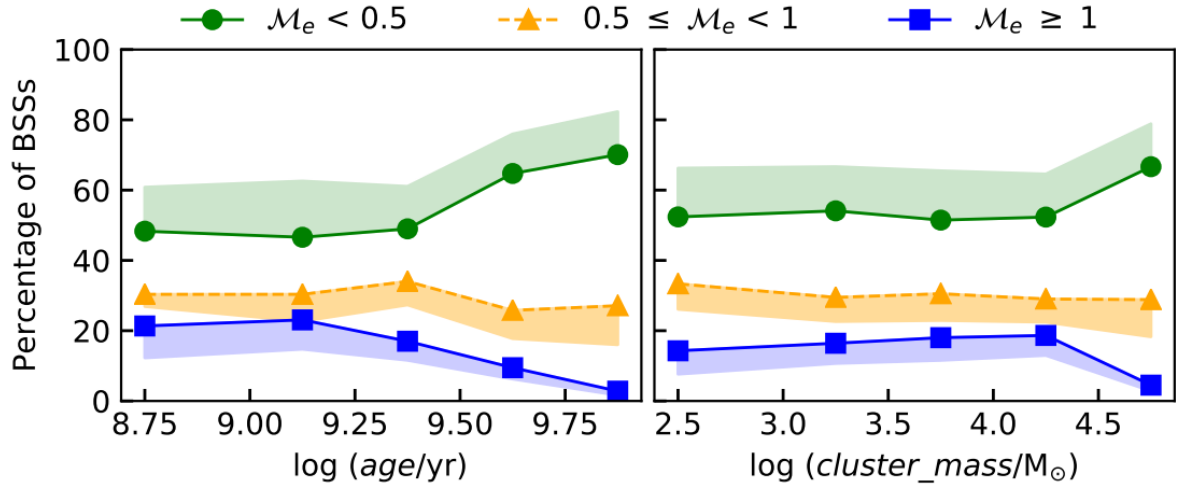

Figure 2.16: Left: Percentage of BSSs to the total number of stars against age. Right: Percentage of BSSs against the cluster mass. Green line indicates BSSs that most likely formed via mass transfer. Fig. 6 from Jadhav & Subramaniam (2021)

2.3 Computational Methods

2.3.1 BPASS[3]

This thesis attempts to recreate Leiner & Geller's (2021) tests using BPASS, as we expect to see that results differ from rapid evolution code. The Binary Population and Spectral Synthesis (BPASS) is a detailed stellar evolution code. It evolves single stars, but also models binary interactions with realistic period and mass ratios (Eldridge et al., 2017; Stanway & Eldridge, 2018). The difference between detailed and rapid stellar evolution models is that rapid population models use pre-made models without updating the model as it evolves. Instead, they use fitting formulas to calculate mass transfer, angular momentum loss and other parameter changes, which is much faster but does not allow to track the changes to the stellar interior (Breivik et al., 2020). BPASS models, however, follow mass transfer from one star to another and the consequent loss of angular momentum of the primary, and it updates the change in the internal structure of the star. This approach allows for predicting stars that single star models do not predict. A specific case of binary interactions that cannot be predicted by single star models are blue stragglers, and BPASS shows good accuracy in predicting their position on the CMD. Fig. 2.19 compares a binary model CMD on the left and a single star model on the right. The left CMD shows dark areas where observational blue stragglers are, while single stars do not have anything in that area.
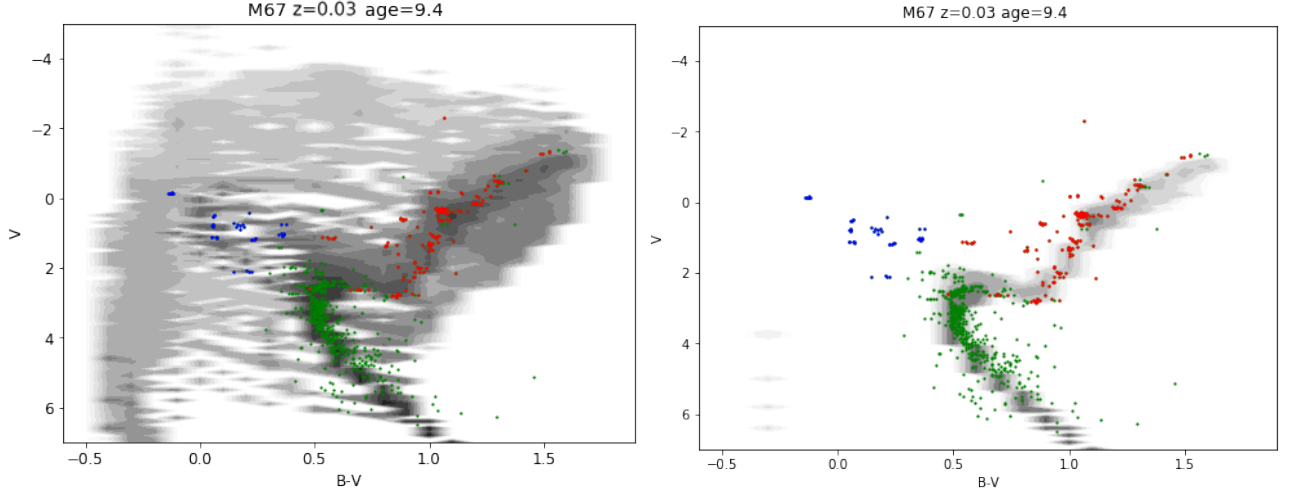
Figure 2.17: M67 open cluster detailed CMD with observational data from the WEBDA catalogue. Main sequence stars in green, red giants in red, blue stragglers in blue. Left: Binary model CMD; Right: Single model CMD. Grey contours indicate the probability density of stars being in that area. Blue stragglers are not predicted with single star models.

BPASS model files vary by metallicity, initial mass of the primary, initial mass of the secondary and the period of the binary. The models follow the whole evolutionary process of the system, but records mainly the important moments of evolution when a significant change occurs, which

---

[3]https://bpass.auckland.ac.nz/

28

is determined dynamically during run-time. Fig. 4.33 shows the evolutionary track of a binary star along with radius and mass sampled by code. There is enough detail to fully represent the CMD, but the data points are not spread evenly in time. BPASS updates the model in timesteps that correspond to a certain number of years, but how large the timesteps are depends on how quickly the star evolves. If not much is happening in the model, then each timestep will be hundreds of thousands of years, but when the star is transferring mass or is going through important points of evolution, then the timestep decreases to capture the details.

Mass transfer in binary systems is modelled according to the Hurley et al. (2002b) prescription, via Roche-Lobe overflow (RLOF). The radius of the RLOF is given by Eq. (2), assuming a circular orbit. When the radius of the primary (R_1) gets larger than the Roche-Lobe radius, mass is transferred onto the secondary. The mass transfer rate is then chosen such that $R_1 = R_{L1}$,

$$\dot{M_{1R}} = F(M_1)[\ln(R_1/R_{L1})]^3 M_\odot yr^{-1} \tag{11}$$

Where

$$F(M_1) = 3 * 10^{-6}[\min(M_1, 5)]^2 \tag{12}$$

chosen so that the mass transfer runs steadily, with radius only just overfilling Roche-Lobe [Eq. 58 and Eq. 59 in Hurley et al. (2002b)]. This mass transfer occurs at a nuclear timescale, but the mass that the secondary can accrete is limited by its thermal timescale, i.e. $\dot{M_2} \leq M_2/\tau_{KH}$, and the rest is lost from the system (Eldridge et al., 2017). This project uses models with the initial mass function (IMF) 135-300 $M_\odot$. The initial mass function tells us about the distribution of masses in the population and is described by a power-law series based on Kroupa et al. (1993) with a slope from 0.1 to $0.5 M_{sol}$ of -1.30 which increases to -2.35 at higher masses.

$$N(M < M_{max}) \propto \int_{0.1}^{M_1} \frac{M}{M_{sol}}^{\alpha_1} dM + M_1^{\alpha_1} \int_{M_1}^{M_{max}} (\frac{M}{M_{sol}})^{\alpha_2} dM \tag{13}$$

(Stanway & Eldridge, 2018)
Where $M_1 = 0.5, M_{max} = 300, \alpha_1 = -1.30$, and $\alpha_2 = -2.35$.

Each model has a N_{imf} parameter which reports the number of such systems we expect per $10^6 M_\odot$ (Stanway & Eldridge, 2018).

29

Parameters of the system that are most important for this study are: 1) masses of primary and the secondary, so that we can track the mass transfer in the system, as well as the mass lost out of the system. 2) radii and separation of the star allow us to observe the evolution stages and how the star reacts to lost/accreted mass. 3) Roche-lobe overflow rate, which tells us the stability of the mass transfer. 4) N_{imf} – Number of similar systems per $10^6 M_\odot$. 5) photometric colours, temperature and luminosity allow us to plot the evolutionary tracks of the system.

2.3.2 hoki[4]

hoki is a python package developed by Stevance et al. (2020b) that makes the BPASS data products and stellar library accessible through python. In this project we have used it to create and plot the CMDs (Fig. 2.19). Each CMD is a grid of cells; the value of each cell depends on how many star systems, weighed by their N_{imf} parameter, fall in that colour-magnitude range, and the higher the number of stars in the cell, the darker it is shaded. The CMD object also has 51 time bins ranging from log(age)=6 to log(age)=11. hoki also has a model data compiler, used to filter BPASS models by certain conditions (e.g. select a range of initial mass or select models with stable mass transfer) and put them into a pandas dataframe. One of the main goals of this thesis is to test BPASS binary models to see how well they can recreate observed BSS populations, and for that we need to classify which stars are blue stragglers and calculate the number of blue stragglers. But as all star clusters are different in size, to count the percentage of BSSs in the star cluster we divide the number of BSSs by the number of red giants. We chose red giants to normalise the BSSs for two reasons.

1. First, the number of BSSs in a cluster is normally very low compared to the total number of stars, the ratios would be much smaller and harder to track as it would be hard to constrain the cluster from the background and foreground stars precisely.

2. But the main reason is that we suppose most blue stragglers form from low mass red giants (proposed by McCrea (1964)). The age constraint (blue stragglers are observed at older ages) and the observed masses of blue stragglers (1-2 times the mass of MSTO stars) suggest low-intermediate ($1M_\odot$ - $5M_\odot$) donors. Gosnell et al. (2015) identify BSS companions in the NGC188 open cluster using the data gathered from the Hubble Telescope. They found blue straggler + white dwarf binaries that formed via a recent mass transfer, indicating that the original donor is a red giant or asymptotic giant branch star, as these are the stars that evolve to become white dwarfs.

---

[4]https://heloises.github.io/hoki/CMDs.html

By definition, blue stragglers are bluer and brighter than MSTO stars. MSTO is the point where main sequence stars start evolving to red giants turning Red on the colour-magnitude diagram. To find the percentage of BSSs to red giants, we must define where on the CMD BSSs are. Most papers rely on isochrones to define MSTO either as the bluest point of the isochrone, or the brightest and bluest point on the MSTO, which often appears as a "hook". Fig. 2.19 shows a CMD with an isochrone over the synthetic CMD from `hoki`, the leftmost point of it marks the MSTO. Because of the way hoki bins the models to display them on the CMD, taking the bluest point on the single star models CMD would, at certain ages, covers a wide range of magnitudes, some being too faint for BSS candidates. So we employ two methods of determining the blue straggler region.

1. By plotting the single star models only on the CMD we obtain a distribution of stars similar to an isochrone for that age and metallicity. We find the colour ($B - V_{\mathrm{MSTO}}$) and magnitude (V_{MSTO}) of the bluest and brightest point of the main sequence. From there, on the binary plot we include points such that $B - V < B - V_{\mathrm{MSTO}}$ and $V < V_{\mathrm{MSTO}} - 1$. The cutoff of magnitudes is such that we include stars brighter and bluer than most of the MS at all ages, at the same time, the white dwarf stars that are located in the bottom left of the CMD do not contaminate our predictions of blue stragglers, as they would not be bright enough. This approach is similar to how Leiner & Geller (2021) define the blue straggler region, which is convenient for the comparison of BPASS results to the four MT stability criteria. Fig. 2.19 shows an example of the regions defined.

2. The advantage of BPASS is that CMDs show the distribution of population beyond what can be seen with an isochrone. Since blue stragglers are a product of binary interaction, we can observe them on the binary CMD as the darker area to the left of the main sequence (Fig. 2.20). This helps to see that the -1 magnitude below MSTO does not completely cover the blue straggler region, moreover, the MSTO region changes shape with the age/metallicity, so it is difficult to get a magnitude cut-off to fit them all. So we go over the ages where we expect to see BSSs (log(age) 9 to 10) and for each CMD we manually determine the magnitude cut-off as the bottom of the darker area to the left of the main sequence.

To ensure that we do not count single star models into the BSSs counts we do not include the parts of the binary CMD that are not empty on the single star CMD. This way, none of the single MS stars are counted as BSSs.[5] We then sum up the N_{imf} for all CMD grid cells within the BSSs limit and the RGB limit.

We define the red giant area as being brighter and redder than the end of the H-R gap, which is a short-lived area on the CMD where main-sequence stars core contracts before it can start burning helium.

---

[5]For the purpose of keeping the N_{imf} of BSS and red giants consistent between ages the weighting by age, applied in `hoki` has been removed

An example of the CMD plot with BSS and RGB regions mapped out using method 2 is shown on Fig. 2.19 and 2.20. We add up the N_{imf} from each cell of the CMD in these two regions separately, which gives us the number of blue stragglers and red giants in the population of 10^6 $M_\odot$ stars. The ratio of BSSs and RGB stars is given below each CMD. To obtain the distribution of the ratio with age we repeat this process for log(age/yrs)= 8.5-10 in 0.1 intervals, as these ages are where BSSs have been generally observed[6]. The selected ages also allow us to avoid mixing the population of blue giants seen in younger clusters, with blue stragglers. Unlike blue stragglers, blue giants are single stars on the horizontal branch. From the Gaia Dr2. observations we see that the BSSs ratios are constant and very low in young clusters, which is confirmed by the BPASS models, as there is almost no dark area to the left of MS until log(age)=8.6. Fig. 2.18 shows 3 synthetic CMDs at log(age/yrs)=8.3, 8.5 and 9, where the blue area highlights regions where BSSs are most probable according to the model.

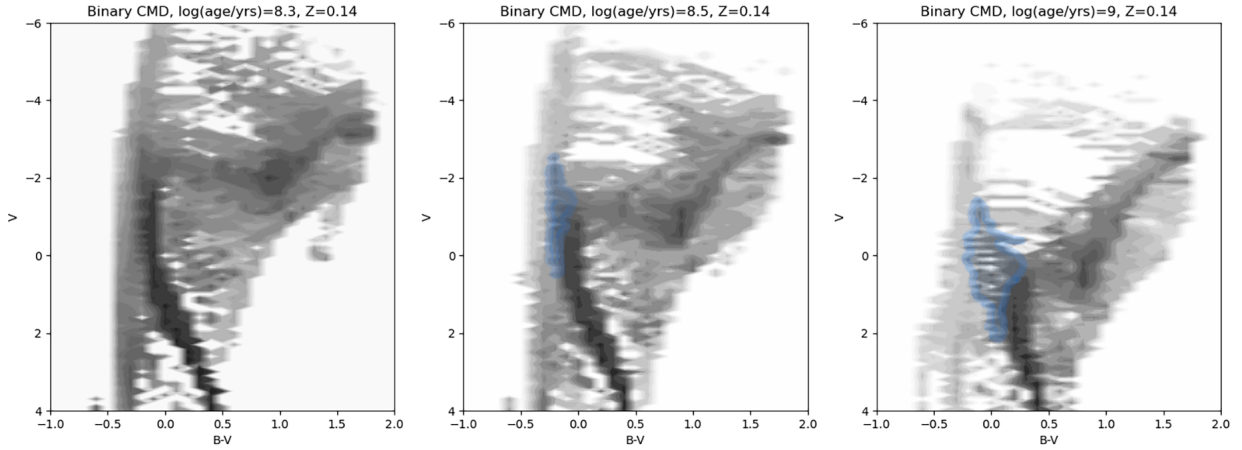Figure 2.18: Three synthetic CMDs at log(age/yrs) 8.3, 8.6 and 9 respectively. Highlighted in blue is the BSS region. At log(age/yrs)=8.3 there is practically no separate region blue and brighter than the main-sequence.

Fig. 2.19 is an example where we use data from the WEBDA catalogue to compare our synthetic CMDs to an observed one. The observed ratio $N_{BSS}/N_{RGB} = 0.28 \pm 0.06$ is 10% larger than the one recorded from the models. This is the systematic error; however, the estimation error would be larger as it depends on how the BSS boundaries are chosen. While the difference between the observed and model ratio is apparent, it is in the right order of magnitude. Comparing that to Fig. 2.20, which contains the observations from the 2MASS catalogue, we observe 16 BSSs and only 39 RGB stars. The modelled and observed ratios are 0.20 and 0.41 ± 0.16 respectively, but in this case the larger observed ratio seems to be due to a low number of red giants. One of the possibilities is that I have chosen too small of a solid angle and cut off when filtering data from foreground and background stars, or the errors on the photometric data of these sources were too large. In general,

---

[6]Code to reproduce results of this study is provided on https://github.com/glebgeinke/Masters-Thesis.git. However you will require BPASS models.

depending on filtering done on the observational data, the 2MASS catalogue contains data on more sources than WEBDA, so the real N_{BSS}/N_{RGB} for M67 is expected to be less than 0.41.
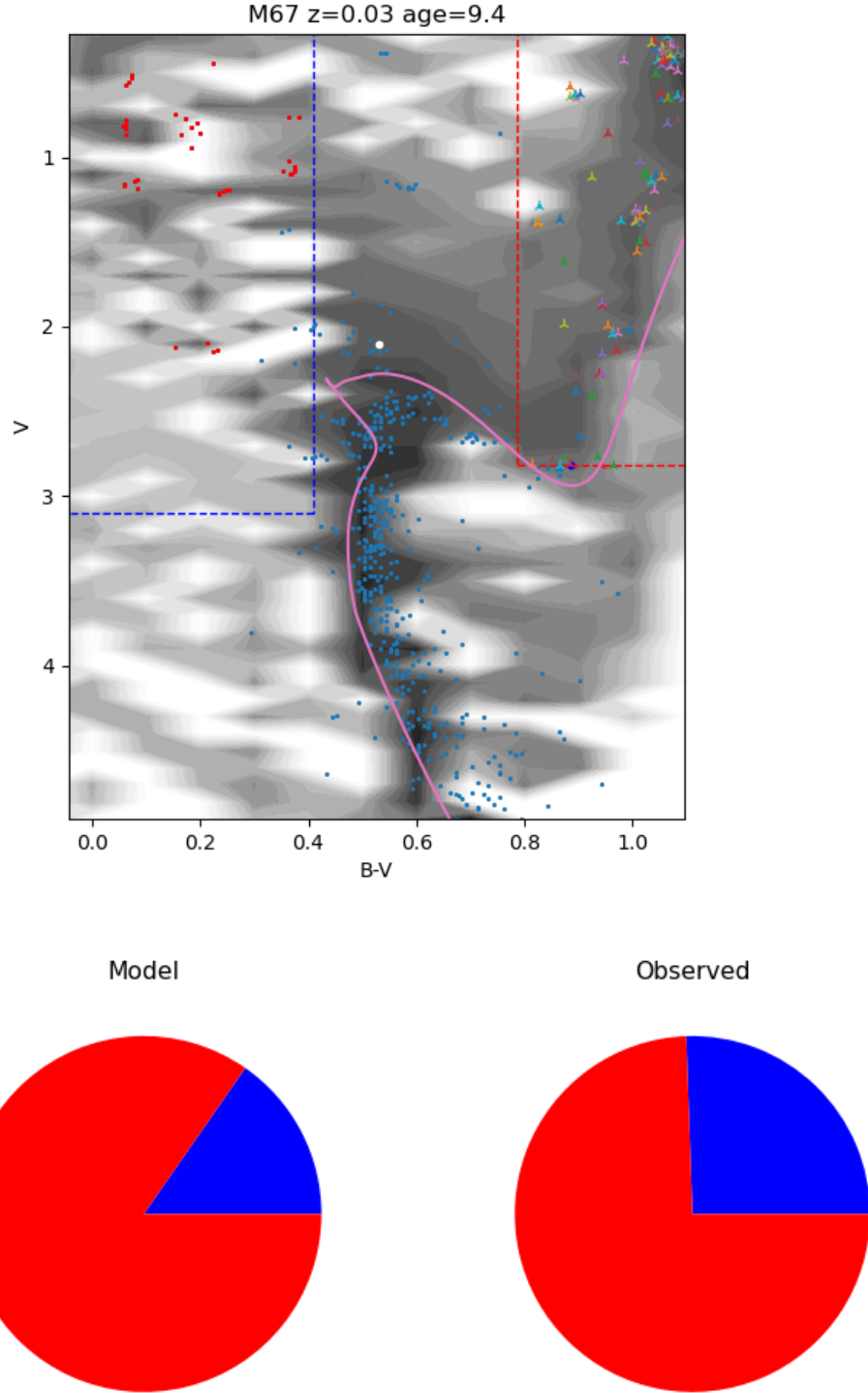

Figure 2.19: Top: M67 open cluster detailed CMD with observational data from the WEBDA catalogue. Blue dashed line represents the BSS region and the red scatter points inside this region are BSSs, Red dashed line represent the RGB stars region and coloured scatter points inside it are RGB stars. Bottom: Ratio of BSSs to red giants from N_{imf} and from observations
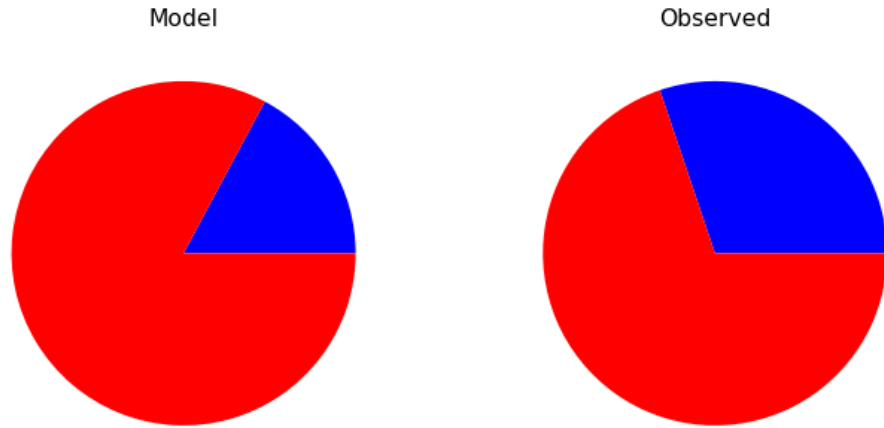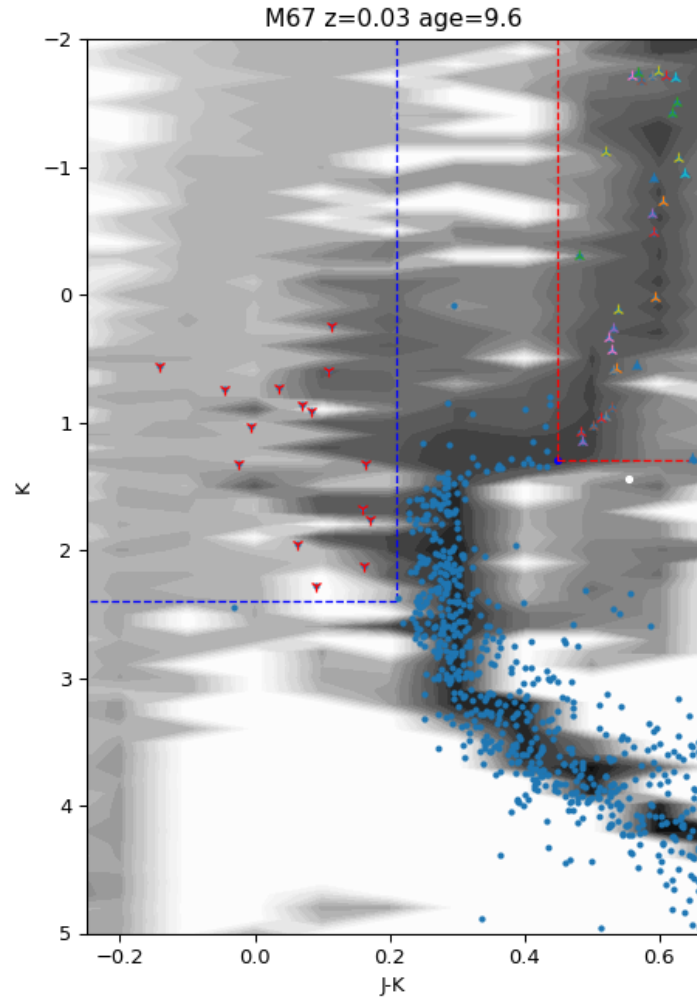
Figure 2.20: Top: M67 open cluster detailed CMD with observational data from the Gaia DR2 catalogue. Blue dashed line represents the BSS region and the red scatter points inside this region are BSSs, Red dashed line represent the RGB stars region and coloured scatter points inside it are RGB stars. Bottom: Ratio of BSSs to red giants from N_{imf} and from observations

3 Results & Discussion

3.1 BSS vs RGB ratio with age

Results of the first method of collecting the BSS vs RGB ratios, where the BSS cut-off is selected as -1 magnitude below MSTO are shown on Fig. 3.23 and Table 3.4, superimposed with the observations from 16 open clusters from (Leiner & Geller, 2021).

There is a clear trend even amongst different metallicities with an increase in the ratio of BSS to RGB stars from log(age/yrs)=9 to log(age/yrs)=9.7, with the exception of z=0.08 which peaks at 9.4. The BPASS results are remarkably close to the observations, and are much closer than mass-criterions from (Hurley et al., 2002b) and (Hjellming & Webbink, 1987), which assumes completely conservative mass transfer, that underpredict the observed values.

When compared to a non-conservative mass transfer, meaning that a lot of mass is lost from the system, points around log(age)=9.2 (1.5 Gyrs) fit well to the observations, but the ratio of BSS flattens out after this point, at approximately $N_{BSS}/N_{RGB} = 0.1$. When the mass transfer efficiency is low, high mass ratio systems can proceed with the mass transfer more stably (Woods & Ivanova, 2011). Underperforming results in this case could be hinting that high mass-ratio systems do not contribute much to the creation of BSSs.

L2/L3 Roche-Lobe with $q_{crit} = 1.8$ (Ivanova, 2015) predicts the q_{crit} of around twice of Hjellming & Webbink (1987). The results for this criterion start with the ratio of BSS to RGB stars being 10% at log(age) = 9, and peaks around 20% at log(age)=9.3. While it is within the error bars for ages 9-9.3, it is clear that this criterion cannot fully explain the increasing trend of BSSs/RGBs with age.

The line indicating No CE shows the BSS/RGB ratio in a case of stable mass transfer at all times. It over-predicts at ages 9-9.3 and underpredicts at ages above 9.5 (Fig. 3.21).

Compared to these stability criteria tested with the COSMIC population synthesis code, BPASS predictions are within the error bars for log ages 9-9.6 (Fig. 3.23 and 3.21), and show a similar trend as the observations, except at metallicity below solar z=0.08. The dependence of the BSS ratio to metallicity has not been widely studied, and we cannot draw conclusions from this data. Fig. 3.22 shows that the ratio increase with age is attributed both to an increase in BSS with age and to a decrease in RGB stars with age, but after log(age/yrs)=9.7 the number of blue stragglers quickly decreases. The match at ages above log(age/yrs)=9.8 is worse, but it is hard to conclude from only two observations. These ages coincide with the helium flash in low mass stars. If helium flash affects the number of BSSs this could be why models struggle to reproduce the increased ratio at these ages.
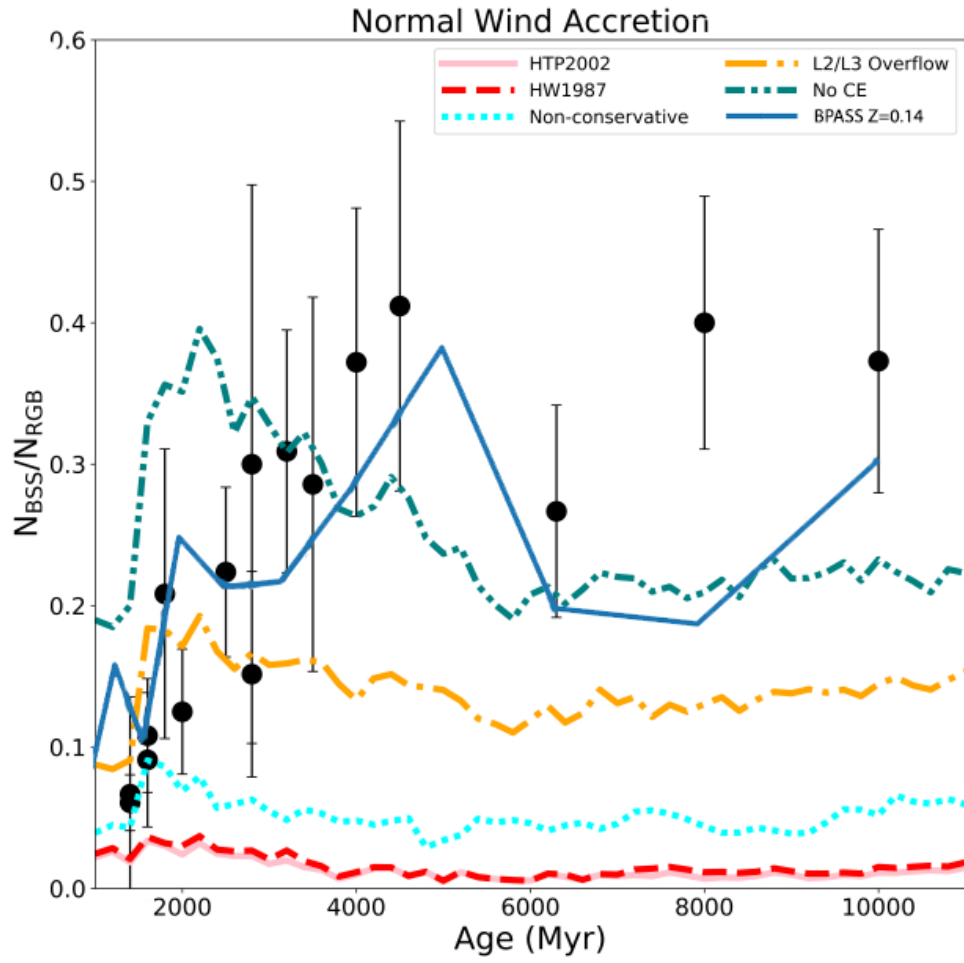
Figure 3.21: Blue solid line shows ratio of BSS to RGB stars with age from BPASS models recorded from the CMDs where BSS region were defined manually. Plotted over the data from Leiner & Geller (2021) for comparison.
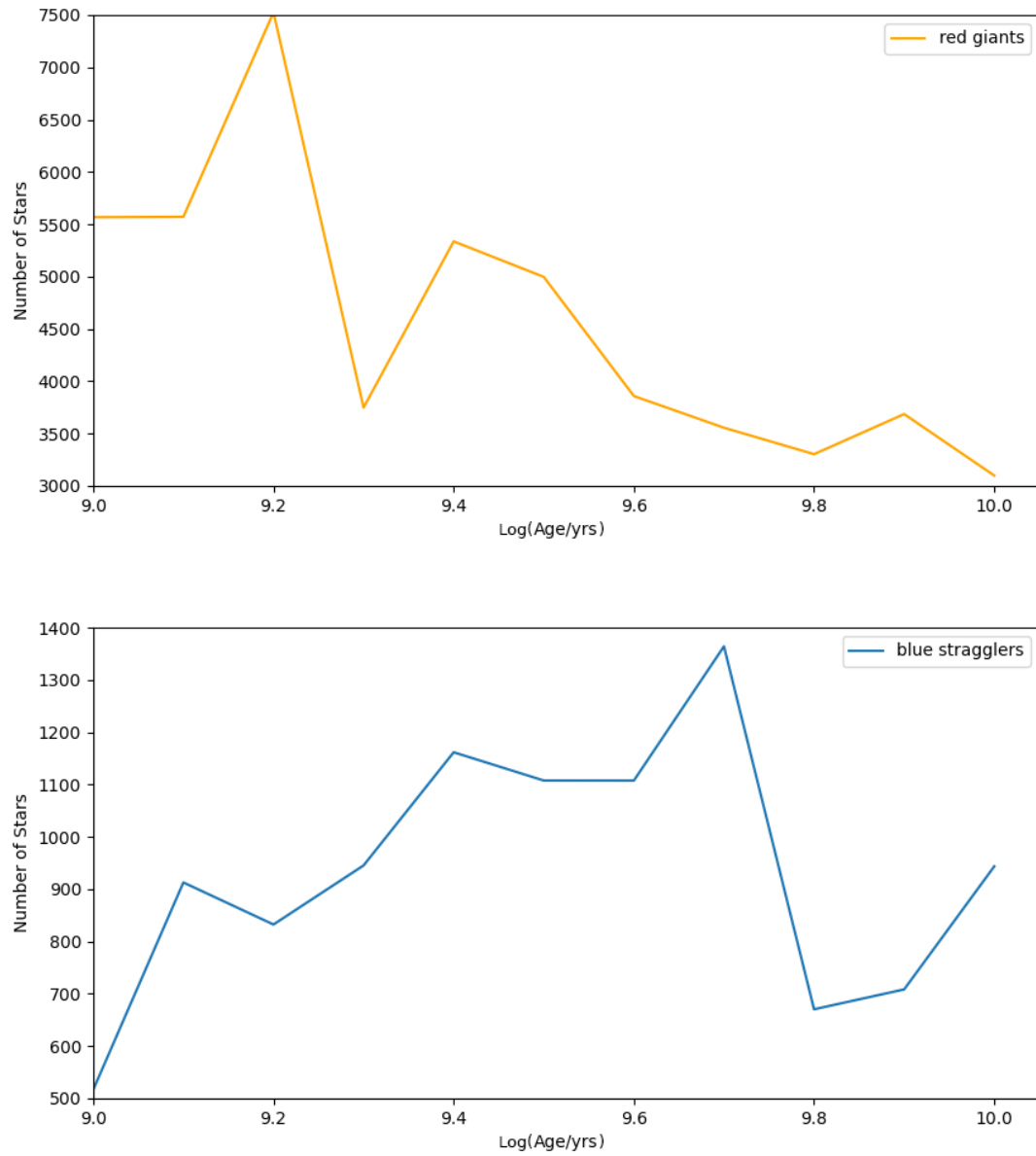
Figure 3.22: Top: Number of RGB stars with age for solar metalicity. Bottom: Number of BSS stars with age.
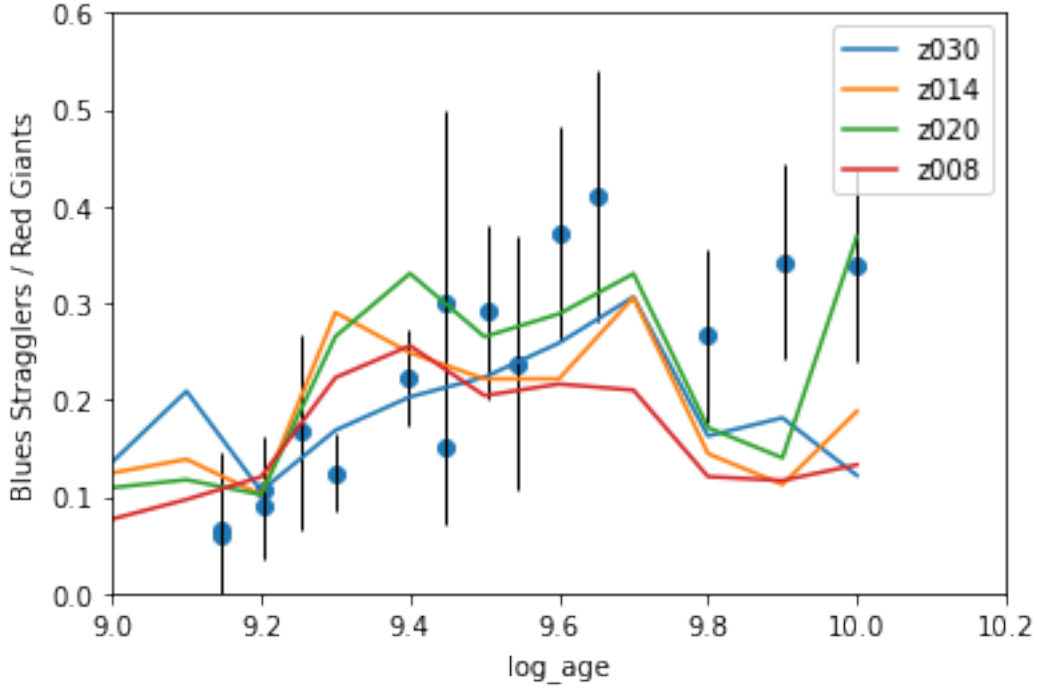
Figure 3.23: Ratio of BSS to RGB stars with time recorded from the CMDs using method [1]. Dots with error bars represent the observations from E. Lenner and A. Gallar

3.2 BSS Count Compared to Jadhav & Subramaniam (2021) Observations

Fig. 3.24 shows the number of BSSs by age compared to observation numbers from Gaia made on 600 clusters (data is binned into log(age)=0.25 bins). The initial bin is broader than the rest, spanning log(age/yrs) 8.5-9. Because BPASS model files contain a population of $10^6 M_\odot$ stars and the majority of the clusters have a mass between $100 M_\odot$ and $100,000 M_\odot$ (Jadhav & Subramaniam, 2021), The observation numbers are scaled to approximately match the number from the models for comparison of the trend with age, as theoretical models populate many more stars than observed clusters had.

Observations from over 800 BSS show a similar trend again: there is a significant increase in the number of BSS from log(age)=9 with the peak of mass transfer BSS numbers between the ages of 9.5 and 9.75 followed by a fall off due to BSSs end of life. Fig. 3.24 on the right shows the total BSSs number peaks at log(age/yrs)=9.125-9.325, which possibly indicates that BPASS produces a larger ratio of mass transfer BSSs to BSSs formed via mergers, as according to Fig. 2.16 the number formed from mergers decreases after log(age/yrs)=9.1. The total number of BSSs has smaller binning (Fig. 3.24 on the right), which unfortunately is not given for stars only in the $M_e < 0.5$ range, hence the binning from Fig. 2.3 in their paper is used.

Fig. 3.24 shows just N_{BSS}, and the trend differs slightly from Fig. 3.23 that shows N_{BSS}/N_{RGB}, with the most noticeable difference being the peak of the z008 line. N_{BSS}/N_{RGB} for sub-solar metallicity starts slowly decreasing after log(age)=9.4, but the number of BSS does not. According to Fig. 3.26, there is a steep increase of RGB stars around log(age) = 9, which does not lead to a proportional increase of BSSs that is observed at different metallicities. While the dependence of metallicity is not deeply studied in this work, Fig. 3.24 and 3.26 may indicate a difference in the formation path between BSSs in solar, super-solar and sub-solar clusters.
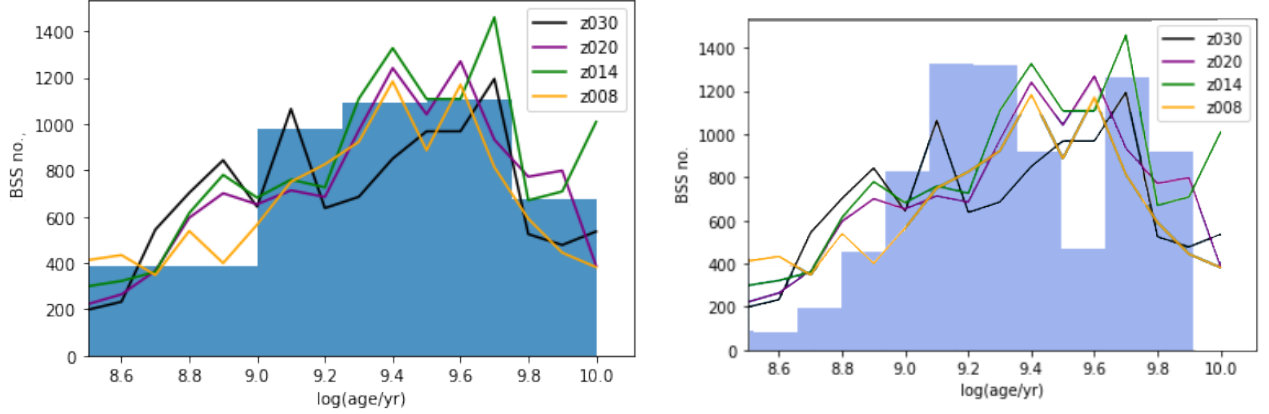
Figure 3.24: Left: Lines show the number of BSS stars from CMDs against age from the models for different metalicities. For comparison, the number of mass transferring BSS ($M_e < 0.5$) from Gaia observations found by Jadhav & Subramaniam (2021) is shown with the bar plot. Right: All observed BSSs ($M_e > 0$) including the mergers. Observations are scaled to match the number of BSSs from BPASS models for comparison.

Figure 3.25: log number of BSS stars from CMDs with time in blue, log number of RGB stars in orange.

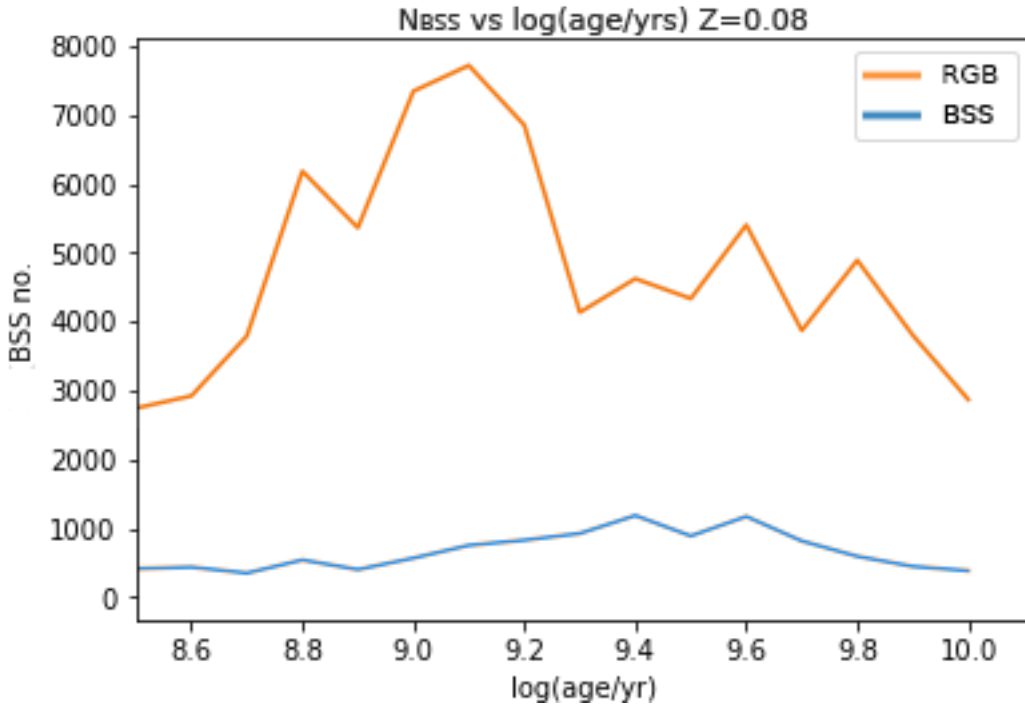|	Z=0.30			Z=0.20			Z=0.14			Z=0.008		
log(age)	N_{BSS}	N_{RGB}	N_{BSS}/N_{RGB}	N_{BSS}	N_{RGB}	N_{BSS}/N_{RGB}	N_{BSS}	N_{RGB}	N_{BSS}/N_{RGB}	N_{BSS}	N_{RGB}	N_{BSS}/N_{RGB}
8.5	197	2487	0.08	299	2664	0.11	221	2299	0.10	412	2741	0.15
8.6	232	2497	0.09	322	2678	0.12	264	2386	0.11	433	2919	0.15
8.7	543	3278	0.17	361	3815	0.09	365	3081	0.12	347	3790	0.09
8.8	702	3858	0.18	615	5493	0.11	595	5284	0.11	538	6181	0.09
8.9	843	5862	0.14	780	5736	0.14	700	6080	0.12	399	5360	0.07
9.0	642	4733	0.14	681	5472	0.12	653	5967	0.11	564	7342	0.08
9.1	1064	5092	0.21	759	5472	0.14	713	6065	0.12	750	7717	0.10
9.2	636	5997	0.11	726	7104	0.10	684	6700	0.10	825	6849	0.12
9.3	685	4058	0.17	1108	3817	0.29	972	3657	0.27	922	4133	0.22
9.4	850	4182	0.20	1327	5335	0.25	1241	3752	0.33	1183	4621	0.26
9.5	967	4329	0.22	1107	4992	0.22	1041	3924	0.27	886	4332	0.20
9.6	968	3739	0.26	1107	4992	0.22	1270	4396	0.29	1169	5401	0.22
9.7	1194	3898	0.31	1460	4772	0.31	932	2820	0.33	813	3868	0.21
9.8	524	3218	0.16	670	4636	0.14	772	4502	0.17	590	4889	0.12
9.9	477	2627	0.18	708	6281	0.11	798	5692	0.14	444	3800	0.12
10.0	535	4390	0.12	1008	5355	0.19	387	1050	0.37	381	2867	0.13

Table 3.4: Number of BSS and RGB stars from N_{imf} of models, that fall into the BSS and RGB regions on the CMDs.

3.3 Models selection

To understand the physics behind why the predictions presented here match better than other mass transfer criteria, we look closer at the models of interest. By reviewing the models that the CMD grid is filled with, we find that the models lying in the BSS area of the CMD range between $M1_{\mathrm{init}} = 0.9$ and $M1_{\mathrm{init}} = 4.5$. Only BPASS models that have experienced Roche-Lobe overflow are selected, and from those, all the stars above $M > 4.5 M_{sol}$ and below $M < 1 M_{sol}$ are removed to look in the mass range of possible mass transfer donor stars. From these models we record the following parameters:

- $M1_{\mathrm{init}}$ – initial mass of the primary

- $M2_{\mathrm{init}}$ – initial mass of the secondary

- M_{tot} – total mass of the system

- He_{core1} – mass of the helium core of the primary

- $\log(age)$ – log(age/yrs) at the time when mass transfer starts

- $\log(R1)$ – Radius of the primary

- $\log(R2)$ – Radius of the secondary

- $\log(a)$ – separation between the two stars

- $\log(P)$ – Initial period of the system

- N_{imf} – number of stars out of the million that fall under this model

- Model type – binary, single star, secondary or a merger.

Then finally, we select the models where the mass of the secondary after mass transfer is greater than the mass of the initial mass of the primary (prior to mass transfer), because these stars will be the ones to appear as BSS in the CMDs. These are the stars expected to really drive the blue straggler formation, as they will be more massive and luminous than the primary stars experiencing post-MS evolution. The results are provided in the 3.5.

$M1_{init}$	log(age/yrs) mean	std dev	end M2 mean	std dev	$M2_{end}/M1_{init}$	$\sum N_{imf}$
4.5	8.13	0.04	6.00	0.99	1.33	174.65
4.0	8.27	0.05	5.44	0.90	1.36	159.90
3.7	8.40	0.04	4.84	0.83	1.31	88.33
3.5	8.43	0.05	4.75	0.86	1.36	152.40
3.2	8.59	0.04	4.23	0.72	1.32	98.24
3.0	8.62	0.07	4.04	0.74	1.35	182.29
2.7	8.79	0.05	3.65	0.61	1.35	131.33
2.5	8.84	0.08	3.41	0.60	1.37	213.05
2.3	9.00	0.05	3.11	0.48	1.35	135.41
2.1	9.07	0.00	2.71	0.39	1.29	61.38
2.0	9.10	0.04	2.78	0.44	1.39	87.99
1.9	9.21	0.00	2.49	0.39	1.31	104.12
1.8	9.28	0.01	2.31	0.37	1.28	155.27
1.7	9.35	0.00	2.16	0.35	1.27	196.23
1.6	9.43	0.00	2.00	0.31	1.25	226.32
1.5	9.51	0.01	1.95	0.31	1.30	318.80
1.4	9.62	0.00	1.77	0.28	1.26	279.44
1.3	9.73	0.00	1.62	0.24	1.25	275.02
1.2	9.85	0.00	1.48	0.20	1.24	280.29
1.1	9.99	0.00	1.33	0.17	1.21	232.46
1.0	10.13	0.01	1.25	0.19	1.25	378.84

Table 3.5: Parameters of stable mass transfer systems: initial M1, mass transfer age, mean M2 after mass transfer, ratio of $M2_{end}/M1_{init}$, and $\sum N_{imf}$, which is the sum of N_{imf} of all systems with the corresponding $M1_{init}$

The age of mass transfer steadily increases as donor mass decreases. This is due to less massive stars spending longer on the main sequence. Most importantly, we see that the N_{imf} suddenly drops around the $M1_{init} = 2.1M_{\odot}$ mark, and then grows as mass goes down to $1M_{\odot}$. At $2.1M_{\odot}$ the mass transfer age is log(age)=9, the age at which an increase in the number of observed BSS starts, shown by the N_{imf} increasing. Another key thing is the ratio of the secondary (the blue straggler)

to MSTO mass, which is given by $M1_{init}$ for the majority of models because mass transfer does not occur before MSTO. If $M2_{final}/M1_{init}$ is high then a lot of mass has been transferred from the red giant to the blue straggler and the star is brighter and hotter than MSTO. This means the blue straggler will be more separated from the top of the main-sequence, but also that the star will burn through the fuel faster compared to stars that only rejuvenated slightly. Table 3.5 shows that stable models in BPASS have $M2_{final}/M2_{init}$ between 1.25-1.4, giving more blue-stragglers in the later ages as the lifetimes are larger.
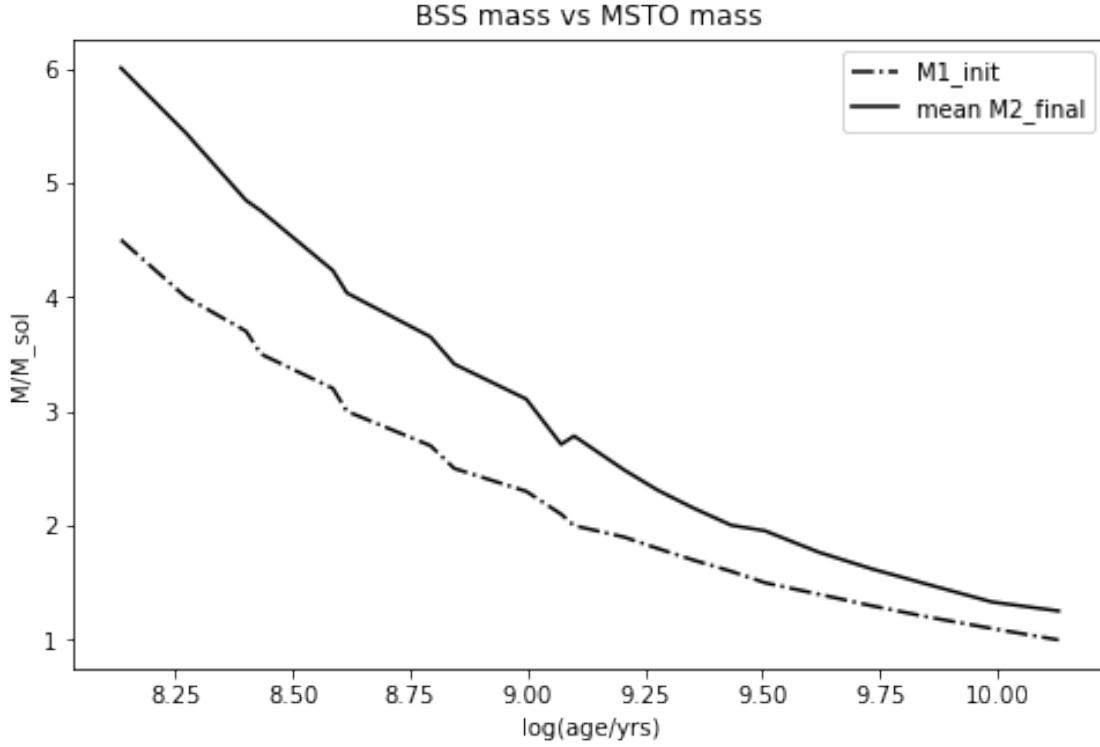

Figure 3.26: Mean mass of secondary after mass transfer shown in solid black line, this represents likely BSSs. Dotted line shows the MSTO mass, given by the mass of the donor before mass transfer. BSS mass is consistently larger by a factor of 1.3.

Let us now consider what happens in the internal structures of stars at the mass transfer stages for those masses displayed in Table 3.5. It is important to consider the internal structure as mass transfer from giant donors with deep convective envelopes is generally more likely to be unstable (Pavlovskii et al., 2016). Figs. 3.27, 3.28, and 3.29 show the mass of the convective boundaries in cyan, and the mass of the H exhausted core in black from the STARS code output files that contain internal stellar structure. BPASS model files are created in STARS code (Eggleton et al., 2011) but do not record the mass of different convective boundaries, hence original plot files are used for more details. The plot shows the surface convective boundary, which is the top cyan line. It covers the mass that is beneath the surface, which is equal to the mass of the star. At the start of each plot at the bottom, the cyan line shows the mass of the convective core.

At log(age/yrs) 8-8.5 there are not many blue stragglers in the models, and mass transfer at these ages happens mostly in stars from $4.5M_\odot$ to $3.5M_\odot$. The internal structure of the donors of $4.5M_\odot$, $4M_\odot$ and $3.5M_\odot$ at these ages (1.34×10^8, 1.86×10^8 and 2.7×10^8 years respectively) indicates that the mass transfer occurred just before the stars develop a deep convective envelope, which happens after the star goes through the Hertzsprung gap. he star starts expanding onto the red giant branch. It is most likely that the star's expansion triggers the transfer of material onto the secondary.
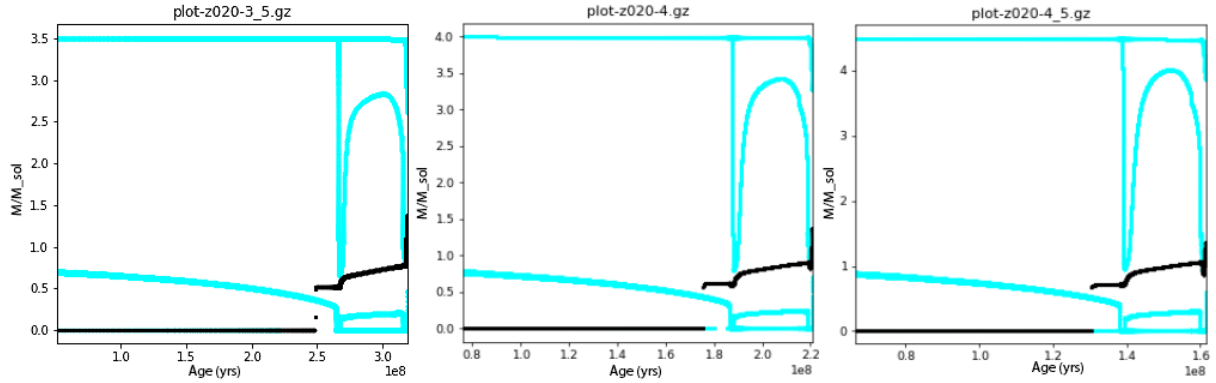

Figure 3.27: Interior structure of single stars from the STARS plot files for $4.5M_\odot$, $4M_\odot$ and $3.5M_\odot$. The y-axis shows the mass coordinates of the convective boundaries, and the x-axis shows age.

For the lower mass stars around $3.2M_\odot$-$2.3M_\odot$, where mass transfer occurs between log(age/yrs) 8.6-9 or 400 Myrs to 1Gyr, the donor is past the Hertzsprung Gap and is cooling down after rapid expansion, and the first dredge-up happened. So the core is now semi-convective, i.e. it is convective in the centre and radiative in the outer core and the envelope, and then again convective at the outer layers of the envelope.
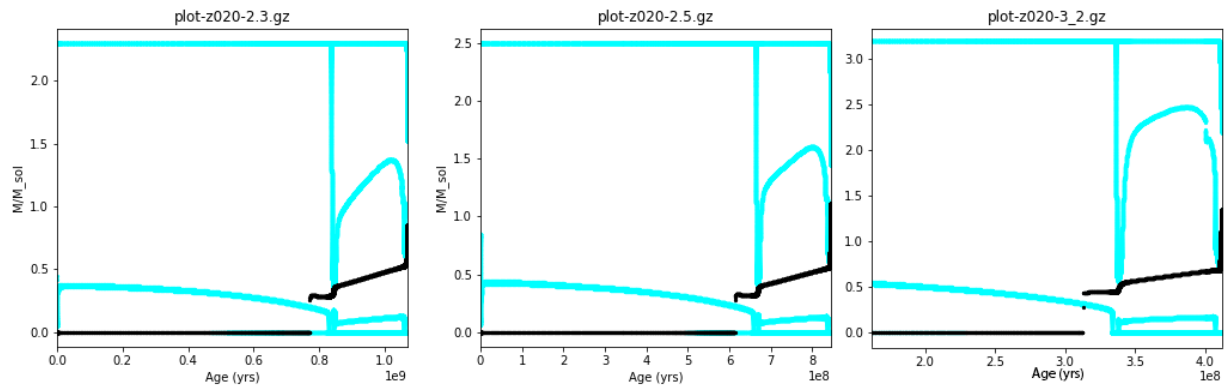

Figure 3.28: Interior structure of single stars from the STARS plot files for $3.2M_\odot$, $2.8M_\odot$ and $2.4M_\odot$. The y-axis shows the mass coordinates of the convective boundaries, and the x-axis shows age.

The largest increase in the number of BSS according to Table 3.5 is at log(age/yrs) above 9, or $M < 2.1M_\odot$. What we can notice from Fig. 3.29 is that at M=2 the mass of the initial convective core suddenly drops from 0.35-0.5 to 0.25. These are the models for which there is an increase in the IMF for possible BSS donors. What can be happening here is that the stars above two solar masses have their convective core contract over their lifetime until they hit the mass transfer stage after hydrogen shell burning. This is delayed in lower mass stars because the cores are below the Schoenberg-Chandrasekhar limit, so they becomes degenerate. Typically the core contracts, heats up and begins helium fusion, causing the star to expand. However, the pressure in a degenerate core is not temperature-dependent, so the helium fusion stage happens much later. The radius of the star is only able to increase smoothly as the hydrogen shell burning continues to increase the mass of the core, so the star mass transfer is much more likely to be stable.
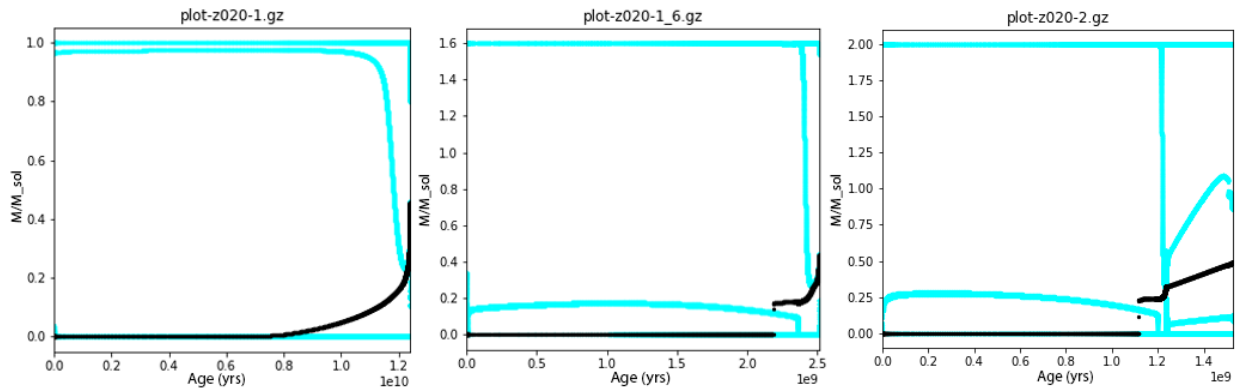

Figure 3.29: Interior structure of single stars from the STARS plot files for $2M_\odot$, $1.6M_\odot$ and $1M_\odot$. The y-axis shows the mass coordinates of the convective boundaries, and x-axis shows age. Convective boundary right outside the core is below 0.25

The comparison of the internal structure at different masses shows us that high and intermediate-mass models, that have deep convective envelopes and short evolutionary timescale between burning stages, produce less stable mass transfer events than lower mass stars. Low mass stars also have deep convective envelopes and should be unstable, but since the core is evolving slowly, there are more mass transfer events and hence more BSSs.

To check the mass transfer stability one can plot log(R1) vs. age of the donor star and the separation between the binaries. In the case of a stable mass transfer via a Roche-lobe overflow the radius of the donor should not exceed the separation between the two stars. When the donor exceeds the separation, a common envelope will form.

By selecting the models where the mass of the secondary after mass transfer is more than $M1_{init}$ we find that all selected models have stable mass transfer, i.e. $log(R1)$ is never larger than separation $log(a)$. Comparing this to all models where mass transfer occurs, we find a lot of models with unstable mass transfer that go through CE. It seems that all models have stable mass transfer below $M1 < 1.3M_{sol}$. Plots showing the radius vs separation of stable and unstable models are given in the Appendix B.

4 Examining Binary Evolution in Details

In the previous section, we examined detailed single star models and how their structure at mass transfer ages could explain the increased number of BSS at later ages. Now we want to look in detail at BPASS binary models and their evolution to determine which models are more likely to lead to stable mass transfer and what type of mas transfer is it.

Fig. 4.30 compares $q = M2/M1$ and $\log(P)$ between models that undergo stable mass transfer (circles) and unstable (triangles). The colour on these plots represents N_{imf} of the model. As mass decreases from $4.5M_\odot$ to $3.5M_\odot$, N_{imf} stays reasonably constant in stable mass transfer models.
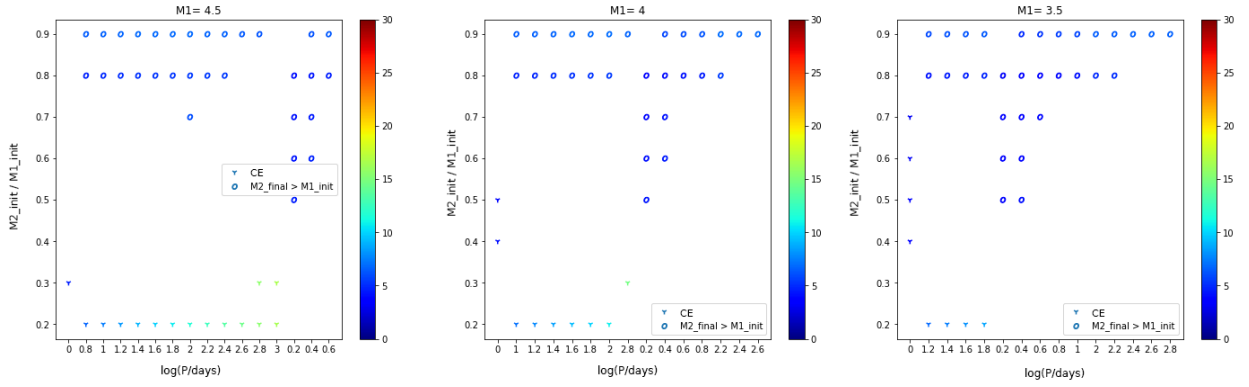

Figure 4.30: Stable and unstable mass transfer model comparison for models between $3.5M_{sol} \leq M1 \leq 4.5M_{sol}$. Mass ratio $q = M2/M1$ on the y-axis, $\log(P)$ on the x-axis. Colour represents the N_{imf} parameter, meaning that redder points represent more stars in the cluster.

In the $2.3M_\odot$ - $3.2M_\odot$ range N_{imf} of separate models increases slightly the lower M1 is, but this mass-range corresponds to mass transfers at ages before $\log(\text{age/yrs})=9$ from which we start seeing an increase in BSS numbers. The summed N_{imf} of the models does not increase according to Table 3.5, meaning that there are fewer models with stable mass transfer than in the higher mass case, but they produce slightly higher N_{imf}.
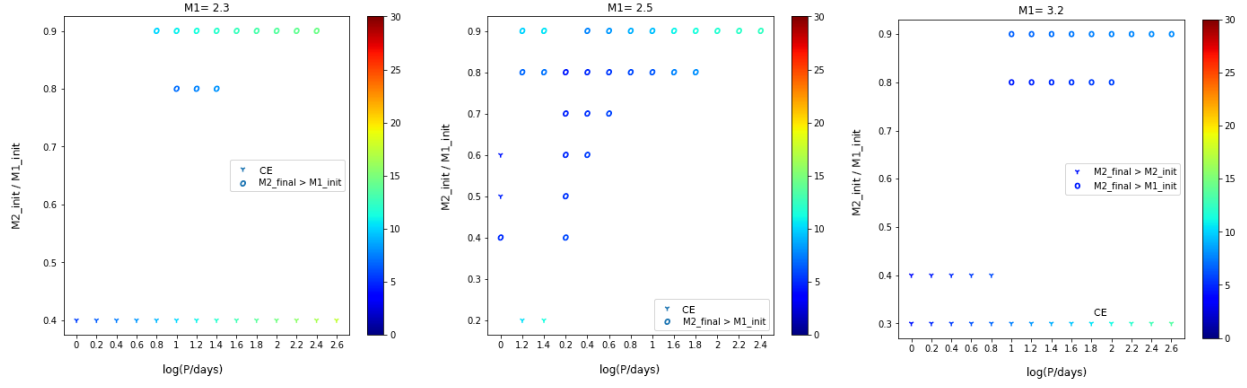
Figure 4.31: Stable and unstable mass transfer model comparison for models between $2.3M_{sol} \le M1 \le 3.2M_{sol}$. Mass ratio $q = M2/M1$ on the y-axis, $\log(P)$ on the x-axis. Colour represents the N_{imf} parameter, meaning that redder points represent more stars in the cluster.

Low mass stars between $1M_\odot$ - $2M_\odot$ also show an increase in the number of stars per model as M1 decreases, but in comparison with the with the $2.3M_\odot$-$3.2M_\odot$ range the increase is significant, with the highest N_{imf} attributed to twin binaries ($q_{\text{init}} > 0.9$) at low masses (M<$1.6M_\odot$) and initial periods in range of 40-160 days, depending on mass. This gives us a good idea of which binary systems contribute the most to the increasing numbers of BSSs at later ages.

The initial mass ratio for unstable mass transfer in almost all cases is low (q=0.2 or q=0.3), meaning that binaries where the primary star is significantly larger than the secondary result in unstable mass transfer and a common-envelope.
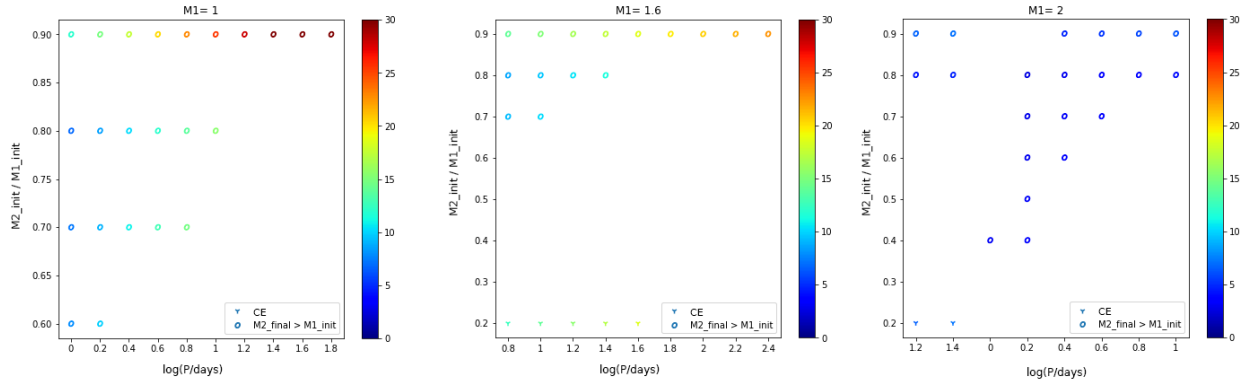

Figure 4.32: Stable and unstable mass transfer model comparison for models between $1M_{sol} \le M1 \le 2M_{sol}$. Mass ratio $q = M2/M1$ on the y-axis, $\log(P)$ on the x-axis. Colour represents the N_{imf} parameter, meaning that redder points represent more stars in the cluster.

Looking at the models with stable mass transfer (where M2 after mass transfer is larger than M1 initial), the mass transfer occurs either during the core hydrogen burning stage (Case A), or post core hydrogen burning (Case B). While BPASS models are not able to track directly whether hydrogen fusion is going on in the shell, BPASS models do not track helium core mass until the hydrogen abundance in the core is very low. This causes a sudden jump in the mass of helium core, which

indicates that core hydrogen burning is over. We examine all models with stable mass transfer at each initial mass of the primary and check whether the moment where the secondary becomes more massive than the primary happens prior to the formation of helium core (Case A), or after it (Case B). The majority of the models undergo Case B mass transfer and Case A only occurs in the higher mass-range.

M_{init}	4.5	4	3.7	3.5	3.2	3	2.7	2.5	2.3	2.1	2	1.9	1.8	1.7	1.6	1.5	1.4	1.3	1.2	1.1	1
Case A	12	9	0	9	0	10	0	11	0	0	6	0	0	0	0	0	0	0	0	0	0
Case B	114	106	77	104	60	89	54	88	45	18	49	48	56	62	66	96	72	75	68	73	89

Table 4.6: Number of models for Case A and Case B mass transfer.

4.1 $4.5 M_{\odot}$ Binary Star

Fig. 4.33, 4.34 and 4.35 show the stages of mass transfer in more detail, along with the radius changes and the evolutionary path. Fig. 4.33 shows Case A mass transfer for the $M1_{init}$=4.5$M_{\odot}$ star. The donor star expands at a nuclear timescale while on the main-sequence, until it reaches the top of the main-sequence, where its radius overcomes the Roche-Lobe radius. Point A marks the start of mass transfer, and we see a slight dip in the orbital separation caused by rapid mass transfer. The Roche-Lobe shrinks slightly in the immediate response to the reduced separation, and the donor is transferring mass at an increased rate on a thermal timescale and is out of thermal equilibrium. The radius of the star does not increase during this period, most likely due to a very high mass transfer rate. The loss of mass causes the luminosity to decrease as the primary crosses the Hertzsprung gap, and a deep convective envelope begins to form. The star requires thermal timescale (4×10^6 yrs) to regain equilibrium beyond the Roche-Lobe, and proceeds to evolve at a nuclear timescale once the equilibrium is reached. When the accreting star becomes larger than the donor, separation and hence the Roche-Lobe radius starts increasing, which switches the mass transfer to being stable. The mass-ratio flip is one of the main reasons why these models produce more stable mass transfer events.

In Section 1.3 we give an example of a single $4.5 M_{\odot}$ star evolution, where at the top of the main sequence the star's core reaches the Schonberg-Chandrasekhar limit and the star's radius more than doubles over 5×10^5 yrs as it cools down the Hertzsprung gap. In this binary case the radius increases smoothly and the Hertzsprung gap period lasts 1×10^7 yrs. It appears that the stripped away mass reduces the pressure on the core not letting it reach the Schonberg-Chandrasekhar limit, i.e. the core does not contract as much; hence the evolution of this stage is not as rapid as in the single case.

Through points B to C hydrogen continues burning in the shell increasing the mass of the helium core; evolution is happening on the nuclear timescale with slow mass transfer. Points C to E, the star is on the RGB, helium burning is ignited in the centre of the core and the radius rapidly increases

and the Roche-Lobe is set in the models to follow the radius so that the mass transfer is steady. However, core mass is not large enough for full helium fusion in the core. On a single star model we see that during the hydrogen shell burning in the core continues to increase until the ignition of helium in the core, which continues fusion until helium is exhausted in the core. In the binary, all of the envelope is stripped before the helium core can significantly increase. As a result, the star becomes a helium white dwarf. This complete stripping of the envelope, including the burning shell, has also been reproduced in other models by Plavec et al. (1973).

There are three stages of mass transfer in Case A mass transfer:
1) initial, fast, thermal timescale mass transfer at log(age/yrs)=8
2) nuclear timescale mass transfer for 150 Myrs
3) second thermal timescale mass transfer at log(age/yrs)=8.4

This means that even higher masses with Case A mass transfer are likely to contribute to the formation of blue stragglers at later ages, but we only see this in approximately 10% of the models at higher masses 4.6.
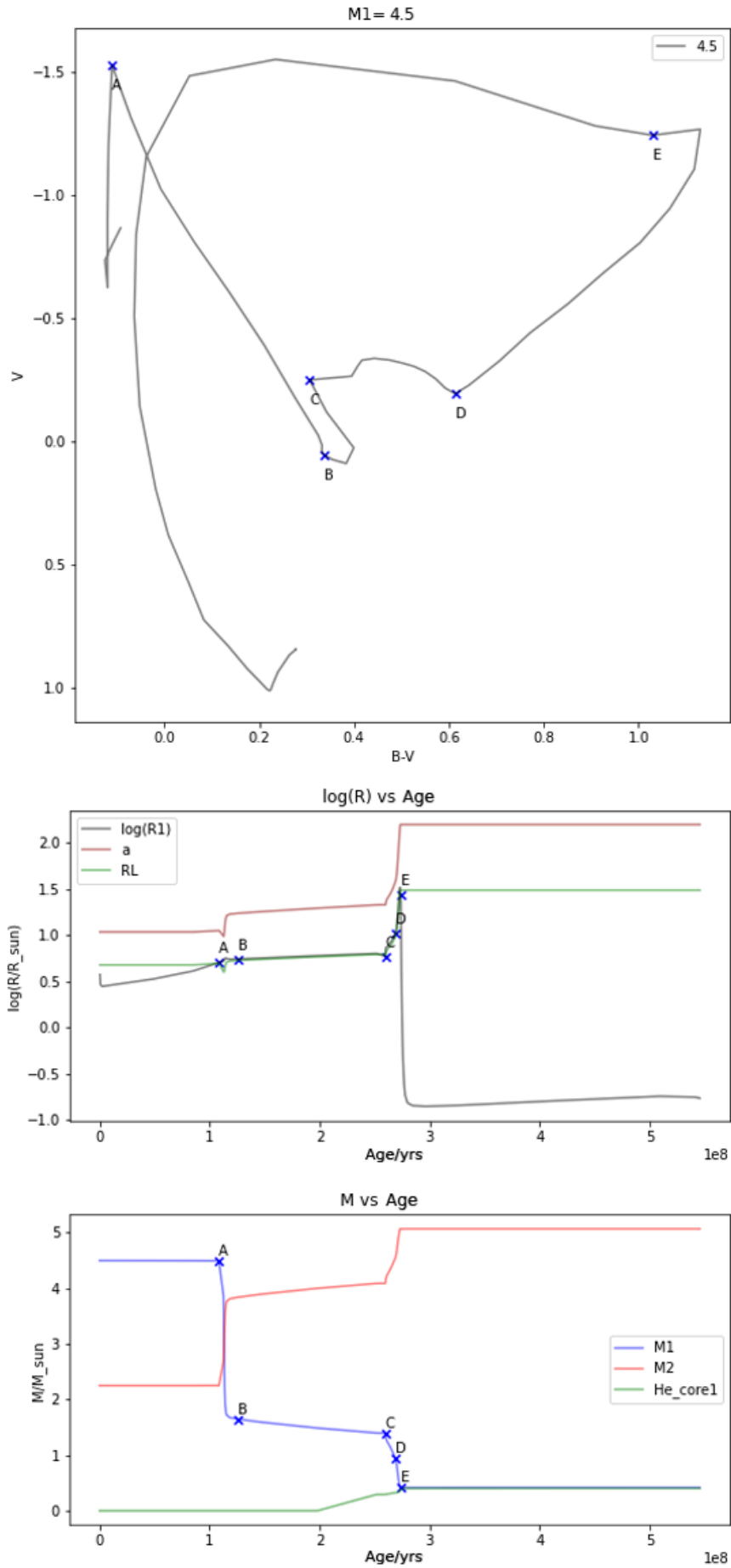
Figure 4.33: Binary evolution of a $4.5 M_\odot$ star. Top: Evolutionary Track; Middle: Radius, separation and Roche-Lobe against age; Bottom: Mass of the donor and its helium core and mass of the secondary against age

4.2 $2.5M_\odot$ Binary Star

Binary evolution of a $2.5M_\odot$ star is very similar to a $4.5M_\odot$ star, also showing a Case A mass transfer but with longer timescales.

   (A) The star reaches the top of the main sequence and hydrogen fusion moves to the shell. Rapid mass transfer starts, but it is not stable as $M_1 > M_2$, so the separation and Roche-Lobe radius decrease, while the radius of the donor does not.

   (B) Mass-Ratios of the two stars flip and $M_2 > M_1$ and mass transfer becomes stable, with Roche-Lobe increasing just enough to fill the radius. Evolution proceeds on the nuclear timescale with steady and slow transfer.

   (C) As the star begins ascending the RGB radius starts to increase quickly further filling the Roche-lobe, so the rate of mass transfer increases again.

   (D) Mass transfer continues until all of the envelope is stripped exposing the hydrogen burning shell. The shell and the core cools down, leaving behind a remnant helium white dwarf.
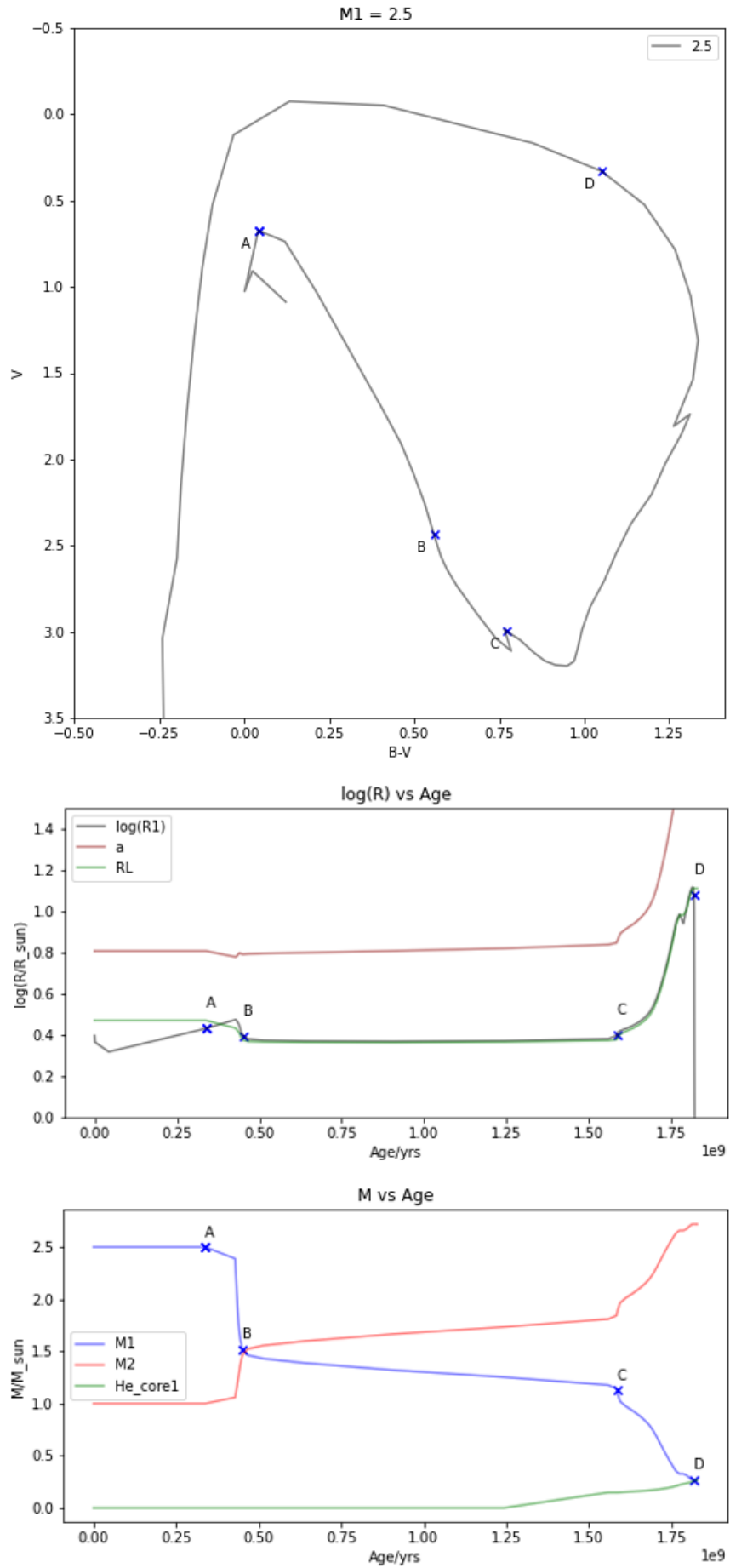
Figure 4.34: Binary evolution of a $2.5 M_\odot$ star. Top: Evolutionary Track; Middle: Radius, separation and Roche-Lobe against age; Bottom: Mass of the donor and its helium core and mass of the secondary against age

4.3 $1.2 M_\odot$ Binary Star

Fig. 4.35 in contrast shows the Case B mass transfer case on the example of a $1.2 M_\odot$ star. Before point A, the star is burning hydrogen in the shell and the radius of the star expands as a result. The core becomes large enough that degeneracy pressure becomes important; until this point, the evolution is identical to a single star. As the star crosses the Roche-Lobe radius at point A rapid mass transfer begins, transferring mass at the thermal scale. The separation between the stars increases and mass transfer is stable. At point B a lot of the envelope is stripped off the donor, but the helium core mass is still increasing, so the shell has not been completely stripped off yet. The luminosity of the star is increasing again until the star is stripped of hydrogen in the shell (point C). Similarly to the other cases, the star becomes a helium white dwarf.

Comparing this to the single model of a $1 M_\odot$ star: the core in the binary model reaches only $0.3 M_\odot$, as opposed to $0.6 M_\odot$ in the single star. All of the mass outside the star's core is stripped before the end of the evolution, so the core cannot expand any further. This means that compared to Fig. 1.2, the binary model does not reach helium ignition, hence does not experience the helium flash.

We are interested in the reason why BPASS is able to get more BSS in the low mass range. Conventionally, mass transfer on the RGB is unstable for high mass models, but we observed that it can become stable at low masses, hence there are more mass transfer events and more BSSs.
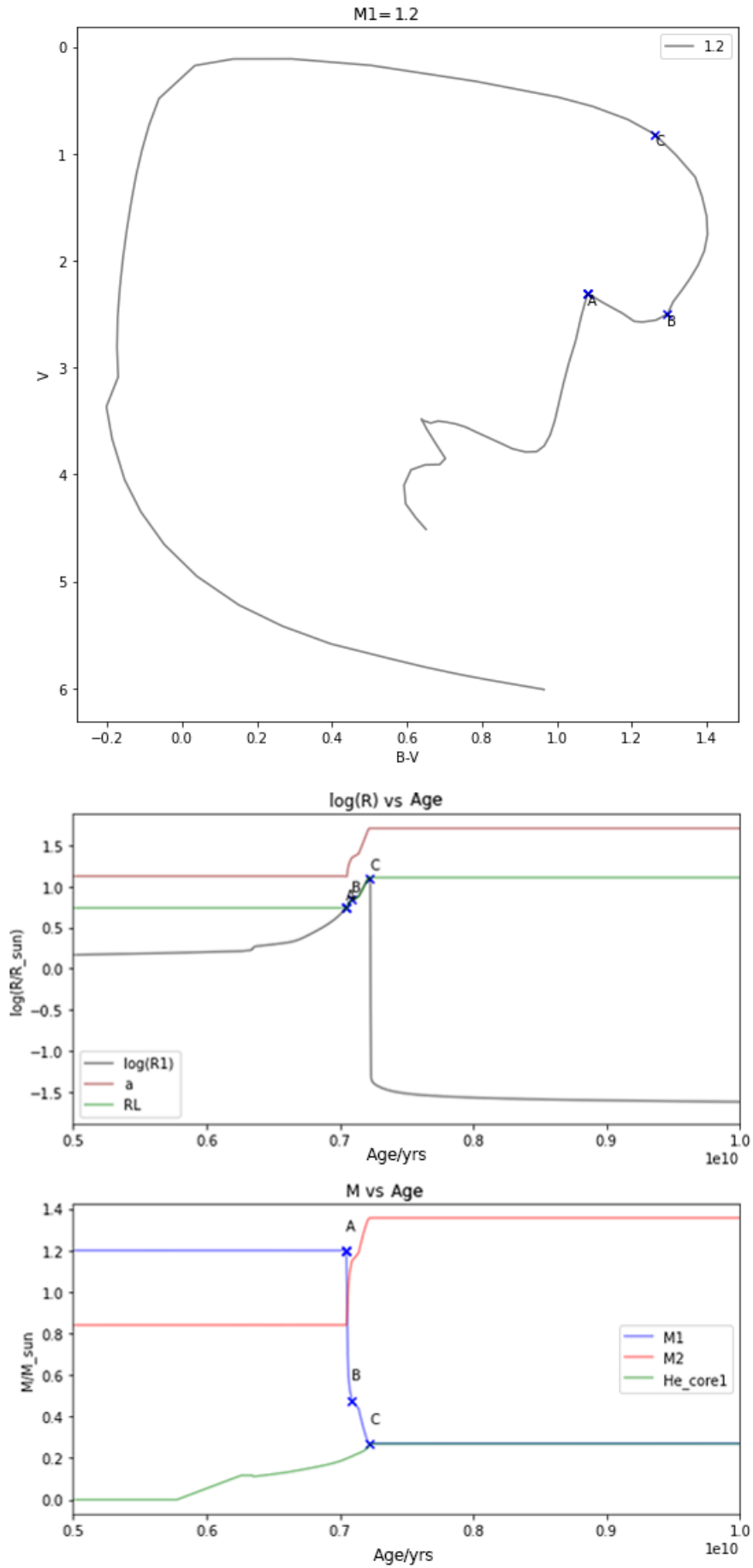
Figure 4.35: Binary evolution of a $1.2M_\odot$ star. Top: Evolutionary Track; Middle: Radius, separation and Roche-Lobe against age; Bottom: Mass of the donor and its helium core and mass of the secondary against age

5 Conclusion

Overall we have demonstrated that BPASS can reproduce the fraction of blue stragglers and red giants at ages above log(age/yrs)=9 much more accurately than rapid population synthesis models with different mass transfer prescriptions (Fig. 3.21). At very old ages, above log(age/yrs)=9.7, BPASS models still underpredict the observations of open clusters; however, only three observations may not be accurately representing of BSS/RGB ratios. While Leiner & Geller (2021) test the Hurley et al. (2002b) prescription that is also used in BPASS, the results are very different due to the way the star responds. It is hard to tell what the results of their comparison would be if they did not multiply the number of red giants by a factor of four, as this number is derived from observations of spectroscopic binaries. However, the BSS to RGB ratio reproduced with the Hurley et al. (2002b) stability criteria in COMPASS is below 0.05, so we do not expect them to be close to what BPASS reproduced even if they did not assume that the number of RGB stars is four times larger. This means that the difference in the result is most likely due to following stellar evolution in detail during mass transfer, rather than relying on approximations.

Models with the most stable mass transfer events were found to be the ones where the mass of the secondary becomes larger than the donor's mass. Models with mean $M2_{\mathrm{final}}/M1_{\mathrm{init}} = 1.3M_{\odot}$ and models with initial mass fractions $q = M2/M1 = 0.9$ have the largest N_{imf}, i.e. they contribute to the number of stable mass transfer events the most. A $M2_{\mathrm{final}}/M1_{\mathrm{init}}$ close to one means that the secondary is more long-lived, leading to more BSSs at later ages. BPASS models show a decreasing number of RGB stars with age, which is another factor that leads to a high N_{BSS}/N_{RGB}. But the most important factor is the initial mass of the donor. We found that models that contribute to the increase at later ages have an initial mass below $2.1M_{\odot}$, and the lower the mass the higher the age of mass transfer and the N_{imf} are.

Most of the stable mass transfer models have over 90% mass transfer efficiency, meaning that less than 10% are lost from the system due to stellar winds. Leiner & Geller (2021) have similar numbers in mass transfer efficiency, so this is not a differentiating factor between detailed and rapid binary population synthesis.

This further confirms that most blue stragglers in open clusters are formed through mass transfer, but dynamical interactions increase in importance at later ages. Case B shows to be the predominant mode of mass transfer with only $\sim 10\%$ contributing from Case A in $4.5M_{\odot}$ - $2.3M_{\odot}$. This can be very different for globular clusters that are more densely populated and have much more tightly bound binaries. In that case we expect there to be more mergers which would produce blue-stragglers.

Looking into the detailed structure and comparing it to single star models there are a few differences. There is a jump in core mass around $2.1M_{\odot}$ and the initial core for lower mass stars is below $M_c = 0.15M_{star}$. Binary models that undergo stable mass transfer have slower and smoother

evolution, as the stars are not able to reach critical pressures, i.e. Schonberg-Chandrasekhar limit for stars above $2M_\odot$ and helium flash, after which stars quickly expand, for low mass stars. If this was not accounted for, then the expansion of the star would possibly cause a common envelope as mass transfer loses stability. One of the possible reasons rapid population synthesis models are not able to replicate this is because they are not updating the stellar structure and therefore cannot tell what is going on with the envelope. A good example shown in BPASS models presented here is the collapse of the envelope, after which mass transfer is stopped as there is nothing to transfer.

Having models that can accurately predict the ratio of blue stragglers to red giants is important to our understanding of mass transfer between binary stars. While single stars have been well studied and are well understood (Eggenberger et al., 2008), binary interactions, on the other hand, alter the evolution of stars and there are no detailed population synthesis models for binaries apart from BPASS. Understanding those interactions better can not only help us determine how many stragglers are in star clusters, but also help us estimate the number of Type I supernovae events, which are responsible for the existence of heavy elements and are used to measure the expansion of the universe. Looking at Type Ia supernova progenitors from the single degenerate channel with these detailed models may reveal more about these stars. It would be good to study the number of mergers BPASS produces at low masses. The next stage of this work will be studying the event rates of Type Ia supernovae and comparing that to existing models and observations.

References

Boffin, H. M. J. Hillen, M. Berger, J. P. Jorissen, A. Blind, N. Le Bouquin, J. B. Mikolajewska, J. Lazareff, B. 2014, A&A, 564, A1

Breivik K., et al., 2020, The Astrophysical Journal, 898, 71

Britannica, William Herschel, https://www.britannica.com/biography/William-Herschel

Crawford J., 1955, The Astrophysical Journal, 121, 71

Efstathiou K., Efstathiou M., 2018, Mechanical Engineering, 140, 31

Eggenberger P., Meynet G., Maeder A., Hirschi R., Charbonnel C., Talon S., Ekström S., 2008, , 316, 43

Eggleton P. P., 1983, , 268, 368

Eggleton P. P., et al., 2011, STARS: A Stellar Evolution Code, Astrophysics Source Code Library, record ascl:1107.008 (ascl:1107.008)

Eldridge J. J., Tout C. A., 2019, The Structure and Evolution of Stars. WORLD SCIENTIFIC (EUROPE) (https://www.worldscientific.com/doi/pdf/10.1142/p974), doi:10.1142/p974, https://www.worldscientific.com/doi/abs/10.1142/p974

Eldridge J. J., Stanway E. R., Xiao L., McClelland L. A. S., Taylor G., Ng M., Greis S. M. L., Bray J. C., 2017, Publications of the Astronomical Society of Australia, 34

Fabio B., Bartholdi P., North P., Burki G., Olson E., 1998, Astronomy and Astrophysics Supplement Series, 132

Gallino R., Arlandini C., Busso M., Lugaro M., Travaglio C., Straniero O., Chieffi A., Limongi M., 1998, The Astrophysical Journal, 497, 388

Geller A. M., Mathieu R. D., Harris H. C., McClure R. D., 2009, The Astronomical Journal, 137, 3743

Gosnell N. M., Mathieu R. D., Geller A. M., Sills A., Leigh N., Knigge C., 2015, The Astrophysical Journal, 814, 163

Hansen C., Kawaler S., Trimble V., 2012, Stellar Interiors: Physical Principles, Structure, and Evolution. Astronomy and Astrophysics Library, Springer New York, https://books.google.co.nz/books?id=GI3qBwAAQBAJ

Hayashi C., Hoshi R., 1961, , 13, 442

Hjellming M. S., Webbink R. F., 1987, , 318, 794

Hollow R., 2022, Introduction to the Hertzsprung-Russell Diagram, https://www.atnf.csiro.au/outreach/education/senior/astrophysics/stellarevolution_hrintro.html

Hurley J. R., Tout C. A., Pols O. R., 2002a, Monthly Notices of the Royal Astronomical Society, 329, 897

Hurley J. R., Tout C. A., Pols O. R., 2002b, , 329, 897

Hurley J. R., Pols O. R., Aarseth S. J., Tout C. A., 2005, Monthly Notices of the Royal Astronomical Society, 363, 293

Ivanova N., 2015, in , Ecology of Blue Straggler Stars. Springer, pp 179–202

Izzard R. G., Hall P. D., Tauris T. M., Tout C. A., 2011, Proceedings of the International Astronomical Union, 7, 95–102

Jadhav V. V., Subramaniam A., 2021, Monthly Notices of the Royal Astronomical Society

Knigge C., Leigh N., Sills A., 2009, Nature, 457, 288

Krane K., Halliday D., Sons J. W. ., 1988, Introductory Nuclear Physics. Wiley, https://books.google.co.nz/books?id=ConwAAAAMAAJ

Kroupa P., Tout C. A., Gilmore G., 1993, , 262, 545

Lamers H. J., M. Levesque E., 2017, Understanding Stellar Evolution. 2514-3433, IOP Publishing, doi:10.1088/978-0-7503-1278-3, https://dx.doi.org/10.1088/978-0-7503-1278-3

Leiner E. M., Geller A., 2021, The Astrophysical Journal, 908, 229

McCrea W. H., 1964, , 128, 147

Miglio A., et al., 2011, Monthly Notices of the Royal Astronomical Society, 419, 2077–2088

Milliman K. E., Mathieu R. D., Geller A. M., Gosnell N. M., Meibom S., Platais I., 2014, The Astronomical Journal, 148, 38

Moe M., Di Stefano R., 2017, , 230, 15

Pásztor E., 2015, Nebra Disk. Springer New York, New York, NY, pp 1349–1356, doi:10.1007/978-1-4614-6141-8_128, https://doi.org/10.1007/978-1-4614-6141-8_128

Pavlovskii K., Ivanova N., Belczynski K., Van K. X., 2016, Monthly Notices of the Royal Astronomical Society, 465, 2092

Plavec M., Ulrich R. K., Polidan R. S., 1973, , 85, 769

Press W. H., Teukolsky S. A., 1977, , 213, 183

Rosenberg H., 1910, Astronomische Nachrichten, 186, 71

Sana H., et al., 2012, Science, 337, 444

Sandage A. R., 1953, , 58, 61

Schönberg M., Chandrasekhar S., 1942, , 96, 161

Seeds M. A., Backman D., 2012, Foundations of astronomy. Cengage Learning

Stanway E. R., Eldridge J. J., 2018, Monthly Notices of the Royal Astronomical Society, 479, 75

Stevance H., Eldridge J., Stanway E., 2020a, The Journal of Open Source Software, 5, 1987

Stevance H. F., Eldridge J. J., Stanway E., 2020b, Journal of Open Source Software, 5, 1987

Verderame L., 2001, Bulletin of the School of Oriental and African Studies, 64, 268

Woods T. E., Ivanova N., 2011, , 739, L48

A   Derivation of Mass Transfer Equations

Kepler's Third Law

We start by deriving Kepler's third law. For a binary system, the total separation is given by

$$a = a_1 + a_2 \tag{14}$$

where from the definition of centre of mass we can equate:

$$M_1 a_1 = M_2 a_2 \quad \Rightarrow \quad a_1 = \frac{M_2 a_2}{M_1} \tag{15}$$

From Eq. (14) we re-arrange for a_2

$$a_2 = \left(\frac{M_1}{M_1 + M_2}\right) a \tag{16}$$

We can now equate the centripetal force and the force of gravity between the two stars in the binary.

$$F_c = F_{grav} \quad \Rightarrow \quad M_2 \omega^2 a_2 = \frac{GM_1 M_2}{a^2} \quad \Rightarrow \quad \left(\frac{M_1 M_2}{M_1 + M_2}\right) a \omega^2 = \frac{GM_1 M_2}{a^2} \tag{17}$$

Substituting for period using $\omega = \frac{2\pi}{P}$

$$\left(\frac{M_1 M_2}{M_1 + M_2}\right) \left(\frac{2\pi}{P}\right)^2 a = \frac{GM_1 M_2}{a^2} \tag{18}$$

After canceling the common terms and re-arranging we arrive to the Kepler's Third law, that describes the relationship between period and separation:

$$\frac{P^2}{a^3} = \frac{4\pi^2}{G(M_1 + M_2)} \tag{19}$$

Change of Angular Momentum

We now want to use Kepler's Third law to show how the momentum changes with the change of mass in the system. From Eq. (19):

$$M_T = M_1 + M_2 \propto \frac{a^3}{P^2} \tag{20}$$

Using the fact that angular momentum for a binary system is $J = M_1 a_1^2 \omega + M_2 a_2^2 \omega$ we differentiate:

$$\dot{J} = \dot{M_1} M_2 \sqrt{\frac{Ga}{M_{\text{TOT}}}} + M_1 \dot{M_2} \sqrt{\frac{Ga}{M_{\text{TOT}}}} + M_1 M_2 \sqrt{\frac{G}{M_{\text{TOT}}}} \frac{a^{-\frac{1}{2}}}{2} \dot{a} - \frac{M_1 M_2 \dot{M}_{\text{TOT}}}{2} \sqrt{\frac{Ga}{M_{\text{TOT}}^{\frac{3}{2}}}} \tag{21}$$

58

Eq. 17 was used to substitute for ω. For a center of mass calculation, angular momentum simplifies to $J = M_1 M_2 \sqrt{\frac{Ga}{M_{\mathrm{TOT}}}}$. We divide Eq. (21) by J.

$$\frac{\dot{J}}{J} = \frac{\dot{M_1}}{M_1} + \frac{\dot{M_2}}{M_2} + \frac{\dot{a}}{2a} - \frac{\dot{M}_{\mathrm{TOT}}}{2M_{\mathrm{TOT}}} \tag{22}$$

This now allows us to derive the equations used in the text and describe what happens to the separation in two cases: conservative mass-transfer and mass-loss.

Separation Change with Mass-Loss

This case describes how the orbit of the binary changes in the case where all mass from the primary is lost from the system, and we assume that angular momentum is conserved, otherwise our binary becomes unbound.

If $\dot{J} = 0$; $\dot{M_1} = \dot{M}_{\mathrm{TOT}}$; $\dot{M_2} = 0$

$$0 = \frac{\dot{M_1}}{M_1} - \frac{\dot{M_1}}{M_{\mathrm{TOT}}} + \frac{\dot{a}}{2a} \tag{23}$$

$$\frac{\dot{a}}{a} = \frac{\dot{M_1}}{M_{\mathrm{TOT}}} - \frac{2\dot{M_1}}{M_1} \tag{24}$$

Substituting for M_{TOT} and re-arranging leads us to the final equation:

$$\frac{\dot{a}}{a} = -\frac{\dot{M_1}}{M_1} \left(\frac{M_1 + 2M_2}{M_1 + M_2} \right) \tag{25}$$

Separation Change with Conservative Mass-Transfer

This case describes how the orbit of the binary changes in the conservative mass-transfer, i.e. all of the mass lost by the primary is accreted by the secondary.

If $\dot{J} = 0$; $\dot{M_2} = -\dot{M_1}$; $\dot{M}_{\mathrm{TOT}} = 0$

$$0 = \frac{\dot{M_1}}{M_1} - \frac{\dot{M_1}}{M_2} + \frac{\dot{a}}{2a} \tag{26}$$

Substituting for M_{TOT} and re-arranging one last time:

$$\frac{\dot{a}}{a} = 2\frac{\dot{M_1}}{M_1} \left(\frac{M_1 - M_2}{M_2} \right) \tag{27}$$

B   Full Plot Data

This section contains the plots used in the paper, but covering more initial masses.

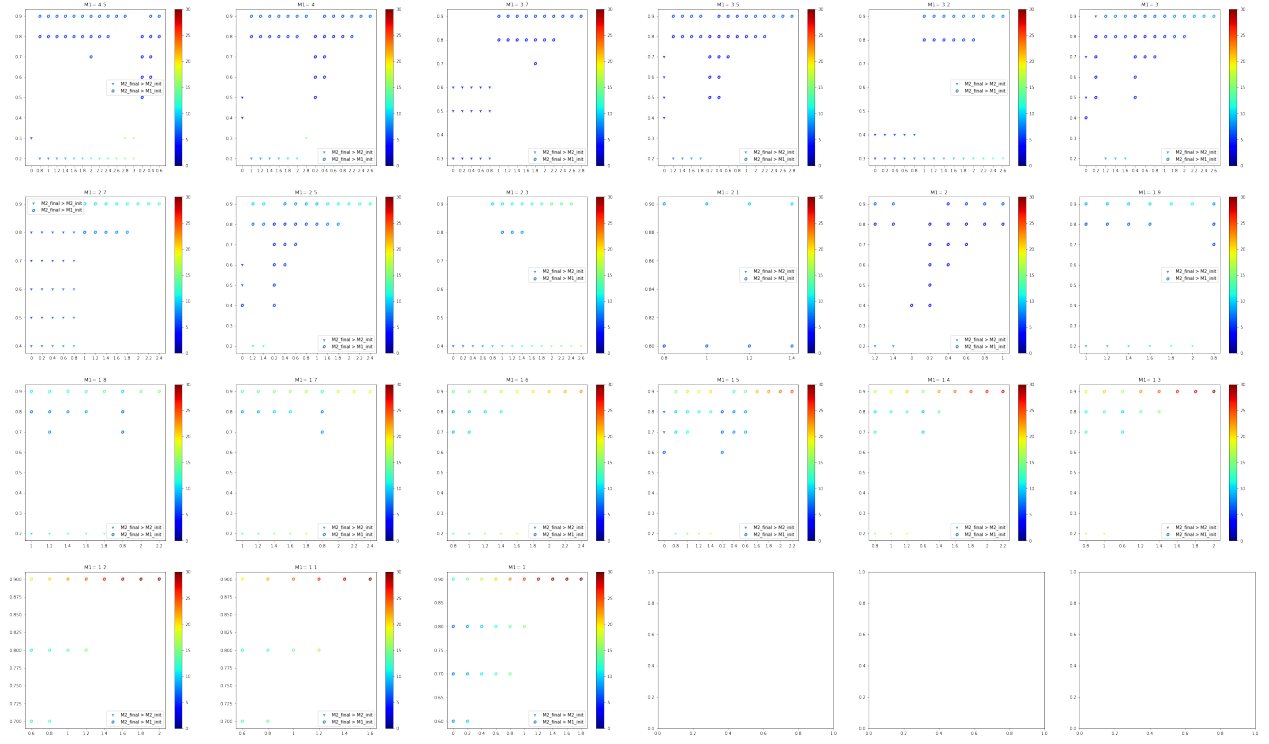
Figure 2.36: Stable and unstable mass transfer model comparison for models between $1M_\odot \leq M1 \leq 4.5M_\odot$. Mass ratio $q = M2/M1$ on the y-axis, $\log(P)$ on the x-axis. Colour represents the N_{imf} parameter, meaning that redder points represent more stars in the cluster.
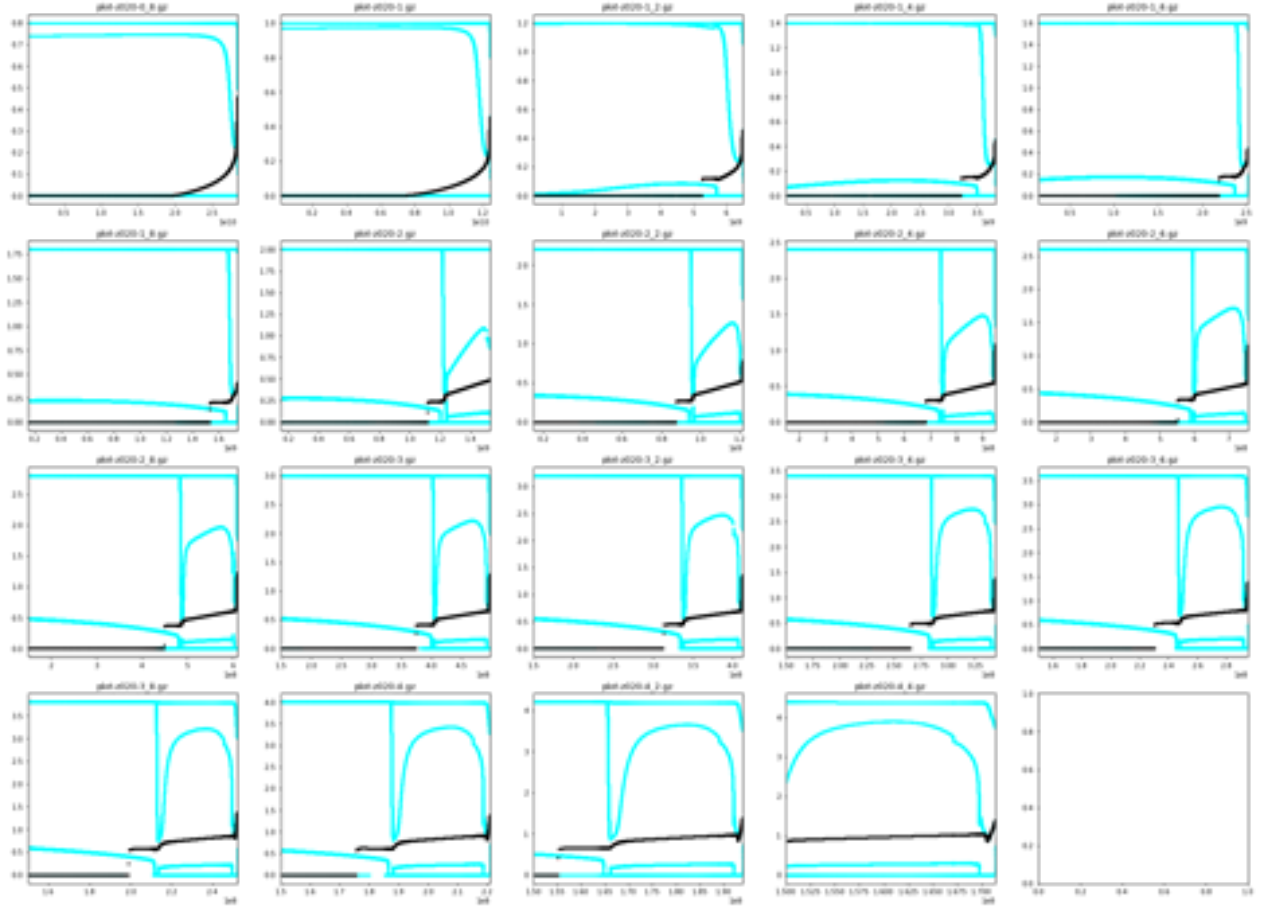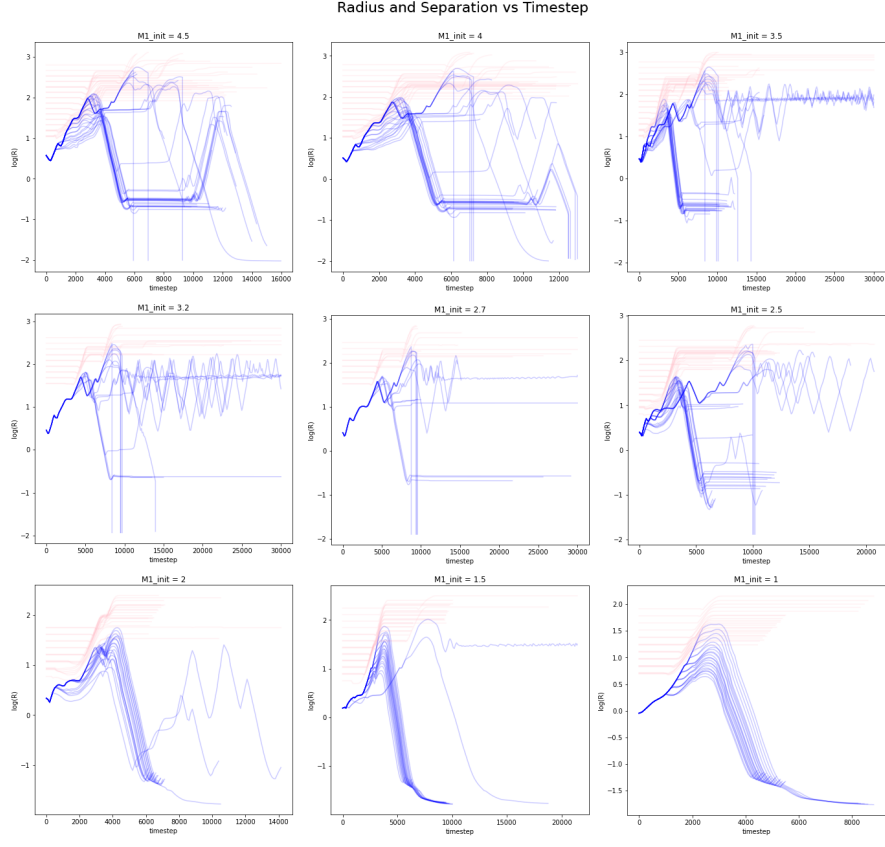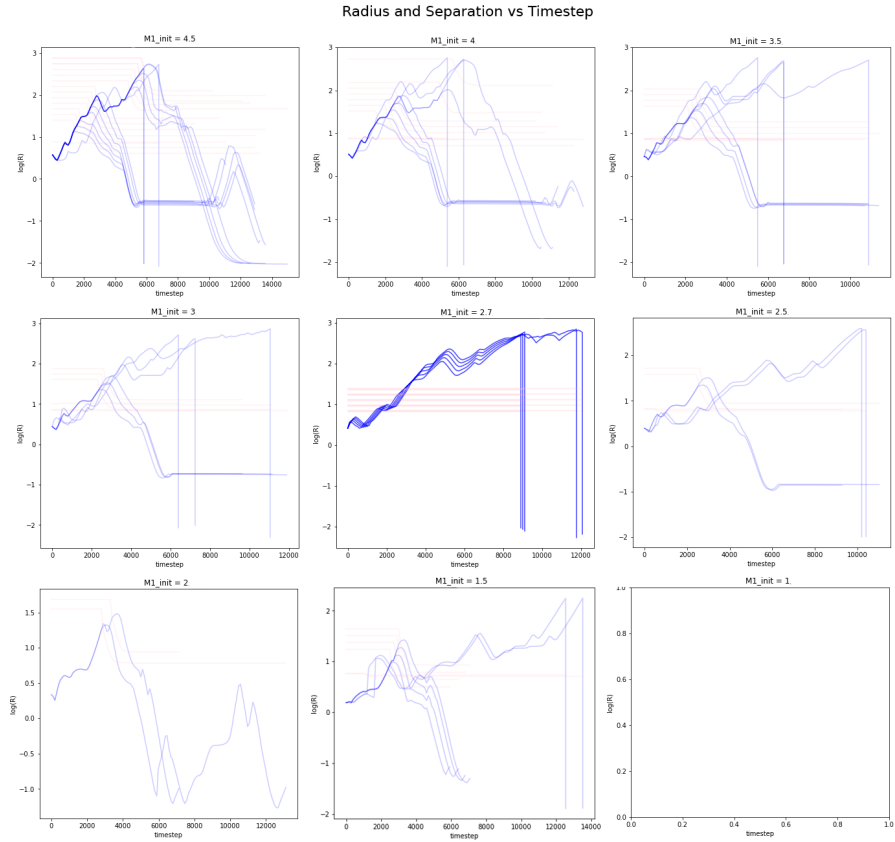
Figure 2.37: Interior structure of single stars from the STARS plot files for $1 M_\odot$ - $4.5 M_\odot$ masses. The y-axis shows the mass coordinates of the convective boundaries, and the x-axis shows age.

Radius and Separation vs Timestep

(a)

Radius and Separation vs Timestep

(b)

Figure 2.38: Radius of the donor star in blue and binary separation in pink plotted against the age of the cluster. a) Only stable mass-transfer models where $M2_{\text{final}}/M1_{\text{init}}$; b) Models where radius overcomes separation therefore forming a common envelope. M1=$2.5M_\odot$ model appears to have numerical errors as separation is constant.

62